isvr Institute of Sound and Vibration Research

A Study into the Feasibility of Using Acoustic Techniques to Locate Buried Objects

B. Papandreou, E. Rustighi and M.J. Brennan

ISVR Technical Memorandum No 979

October 2008

University of Southampton

SCIENTIFIC PUBLICATIONS BY THE ISVR

Technical Reports are published to promote timely dissemination of research results by ISVR personnel. This medium permits more detailed presentation than is usually acceptable for scientific journals. Responsibility for both the content and any opinions expressed rests entirely with the author(s).

Technical Memoranda are produced to enable the early or preliminary release of information by ISVR personnel where such release is deemed to the appropriate. Information contained in these memoranda may be incomplete, or form part of a continuing programme; this should be borne in mind when using or quoting from these documents.

Contract Reports are produced to record the results of scientific work carried out for sponsors, under contract. The ISVR treats these reports as confidential to sponsors and does not make them available for general circulation. Individual sponsors may, however, authorize subsequent release of the material.

UNIVERSITY OF SOUTHAMPTON

INSTITUTE OF SOUND AND VIBRATION RESEARCH

DYNAMICS GROUP

A Study into the Feasibility of Using Acoustic Techniques to Locate Buried Objects

by

B. Papandreou, E. Rustighi and M.J. Brennan

ISVR Technical Memorandum No: 979

October 2008

Authorised for issue by
Professor Michael Brennan
Group Chairman

A Study into the Feasibility of Using Acoustic Techniques to Locate Buried Objects

B. Papandreou, E. Rustighi, M.J. Brennan

Institute of Sound and Vibration Research,
University of Southampton

Abstract

Work has been undertaken with the aim of detecting shallow buried objects using seismic waves. An existing method of time domain stacking, where contributions from various surface sensors are summed based on propagation distance, is expanded upon by the addition of time extended, rather than impulsive, excitation signals. As a consequence of this cross-correlation functions, rather than time domain signals are stacked. Generalised cross-correlation functions, specifically the phase transform, are implemented and shown to enhance detection. Experimental work has been undertaken using a concrete pipe as a target and results are presented. Although the use of shear waves for target illumination is shown to be preferable only compressional and surface waves could be detected at the target, despite the coupling of the shaker to a platform designed to preferentially induce shear vibrations. By stacking compressional waves with the phase transform applied, an image of the target can be produced. This image cannot, however, be produced for every measurement run.

Contents

List of Symbols

A, B	Arbitrary Rayleigh wave component amplitude constants
$\mathbf{A}$	Vector of waveform amplitudes
A_0, V_0	Acceleration and velocity chirp amplitudes
b	Bandwidth of bandlimited signal
c, c_R, c_c, c_s	General wavespeed, Rayleigh, compressional and shear wavespeeds
C	Amplitude scale factor between delayed signals
D	Geophone separation
E	Young's modulus
f	Frequency
f_1, f_2	Start and end frequencies of chirp
f_0	Centre frequency of bandlimited signal
$F(z), G(z)$	Rayleigh displacement potential depth dependence functions
F, F^{-1}	Fourier transform and its inverse
G_{xx}, G_{xy}	One sided auto and cross spectral densities
G	Shear modulus, also called Lamé's second constant
h	Target depth
j	$\sqrt{-1}$
k	Wavenumber
L	Duration of signal measurement
M	Frequency domain amplitude of bandlimited signal
$\mathbf{n}$	Normal unit vector
N	Number of geophones
R_{xx}, R_{xy}	Auto and cross correlation functions
s	Source and sensor separation
S_{xx}, S_{xy}	Two sided auto and cross spectral densities
t	Time variable
T	Chirp length
$u, v, w, \mathbf{u}$	Displacement components, displacement vector
U, W	Rayleigh wave depth displacement functions

V	Volume
$x, y, z, \boldsymbol{x}$	Spatial coordinates, spatial vector
x_s	Surface distance from origin to source
$x_{g,i}$	Surface distance from origin to ith sensor
$x(t), y(t)$	Time histories
α, η	Ratio of shear to compressional & Rayleigh to shear wavespeeds
γ_{ij}	Shear strain
$\gamma_{xy}(f)$	Coherence function
δ_{ij}	Kronecker delta
$\varepsilon_i, \varepsilon$	Axial strain, sum of axial strains
η_1, η_2	Ratio of the angular frequency to compressional & shear wavespeeds
λ	Wavelength
μ	Lamé's first constant
ν	Poisson's ratio
$\xi, \boldsymbol{\psi}$	Displacement potentials
ρ	Density
σ_i	Normal stress
τ	Correlation time lag variable
τ_0	Time delay between signals
τ_{ij}	Shear stress
φ	Phase
$\psi(f)$	Generalised correlation weighting function
ω	Angular frequency
$\boldsymbol{\Omega}$	Rotation vector
∇	Dell, spatial partial derivative operator
$\otimes$	Convolution
$(*)$	Complex conjugation

$(\tilde{\ })$	Hilbert transformed signal
$(\hat{\ })$	Unit vector

Section 1 - Literature Review

The work reported here involves the detection of buried objects at depths in the range of a half a metre to two metres beneath the ground's surface. The method described should be able to detect a wide range of targets. These may include, but are not limited to, large items of ordinance, tunnels and archaeological artefacts. Existing techniques for detection of objects buried in the ground are separated into non-seismic and seismic methods and considered separately in Sections 1.1 and 1.2 respectively. Significant research has been undertaken in recent years with the aim of detecting buried antipersonnel mines. Despite the different depth and size of the intended target, the applicability of these technologies must still be examined to assess their validity in detection of objects buried at the depth specified for this project. Methods for detecting targets in media other than ground are considered in Section 1.3. Despite the different physical characteristics their examination is still useful due to the similarities in post-processing methods.

1.1 - Non-Seismic Methods

1.1.1 - Metal Detectors & Electromagnetic Induction

The metal detector is an established technology and is the main technology used in demining applications [1]. The metal detector utilises the phenomenon of electromagnetic induction in order to detect conductive materials. This concept is well understood and documented [2], and is elegantly encapsulated within Maxwell's laws. These state that a time varying electric field will induce a magnetic field and vice versa.

In a basic metal detector [3] a time varying current is passed through a primary coil, inducing a magnetic field which penetrates into the earth. Any conductive material in the vicinity will experience a time varying magnetic field and thus have current induced within it, with these induced currents referred to as eddy currents. These will induce a second magnetic field which in turn induces a current in a secondary coil within the metal detector. In the simplest case an audio signal is triggered when the current in the secondary coil exceeds a given threshold to alert the operator of the presence of the conductive material.

An obvious problem with the use of this type of detection is that no information is provided as to the nature of the conductive object detected. Thus the basic metal detector is unable to differentiate between objects of interest and the harmless metallic clutter. This is particularly problematic in demining applications where metallic clutter is likely to be prevalent in urban areas and former conflict zones in which the mines are found. Furthermore each detection must be treated as though the object were a target. In severe cases only one in a thousand detections are of objects of interest [1]. This makes the method inefficient and also causes a greater risk to the operators who must attempt to remain rigorous throughout the many false alarms.

Metal detectors are also adversely affected by the type of soil under interrogation. If the soil has notable magnetic properties (such as a permeability significantly greater than unity) then a secondary magnetic field will result from the magnetisation of the material, lowering the signal to noise ratio of the measurement [4]. Furthermore if the there is large spatial variation in the magnetic properties of the material then false alarms may result [5]. If the soil is conductive (for example due to moisture content)

the operation of the metal detector will also be degraded, with both the penetration depth and amplitude of the return signal reduced [6]. In normal operating conditions metal detectors can only find large metallic objects to a depth of about half a metre, and smaller targets such as landmines within the first few tens of centimetres [3]. These depths are reduced further still in the presence of moisture.

Metal detectors have an obvious limitation; they only detect conductive materials. Thus if the target object is non-metallic it will not be detected, regardless of soil conditions or clutter levels. Many mines in use today [7] contain only small amounts of metal, thus posing a problem for metal detectors. Whilst the sensitivity of the metal detector could simply be increased by reducing the threshold level for production of an audio cue this would result in an even greater number of false alarms as even smaller pieces of metallic debris are detected.

In order to improve the rejection of clutter and thus improve the effectiveness of metal detectors modern signal processing techniques may be exploited. It has been suggested that phase information from the returned signal can be used to aid in clutter discrimination [8]. The phase information received can be compared to a database of known object signatures in order to discriminate targets from clutter. Whilst this method could offer promise in some circumstances it has the limitations that the signature of the material must be known, and that the orientation of the target will influence this signature. In cases where the signal to noise ratio is low the method may also be unable to accurately discriminate between object signatures.

A new method for discriminating from clutter is electromagnetic induction spectroscopy (EMIS) [9]. This method uses input magnetic fields of frequency varying over a large bandwidth (30 Hz - 24 kHz) and has been applied specifically with the aim of detecting landmines. The level of eddy current formation within the target has a complex dependency on the materials of which it is composed, its size and orientation. Thus detectable objects have very different levels of response over the frequency range used. Unfortunately the differences in the current induced in the secondary coil are great even between individual types of landmine, and as such there is no common distinguishing feature which allows for discrimination of landmines from clutter. Instead a library of landmine signatures would need to be collected in order to give the method value. This may be difficult as the signatures may vary substantially depending on the environment in which they are situated, and would furthermore prohibit the use of the method for detection of other targets for which there is no existing information.

The technique has been further developed to use a linear array of sensors on a small vehicle mounted platform [10]. This has proved effective at finding targets. However the flaws fundamental to electromagnetic induction remain; limited interrogation depth and inability to detect low metal content targets in noisy environments and challenging soils.

1.1.2 - Ground Penetrating Radar & Electromagnetic Reflection

The operation of the ground penetrating radar (GPR) is as follows [11]. High frequency (of order 1 MHz to 10 GHz depending on the situation) electromagnetic waves are inputted to the system. Reflections of the waves occur at discontinuities or gradients of the permittivity of the material (a parameter associated with its dielectric

properties). Reflections are measured via an antenna located next to the source. There are several different versions of the method, some for example using very short (of order nanosecond) pulses, whilst others use time extended signals whose frequency content is either continuously or discontinuously varying [12].

This method is capable of detecting non-metallic targets as it is the permittivity of the target not its conductivity that results in detection. However this also means that the method is unable to differentiate between clutter and targets of interest. Rocks, tree roots etc. and ground inhomogeneities can cause false detection [13] that reduces the effectiveness of the method.

The conditions of the ground are of key importance. The electromagnetic waves used are attenuated by propagation through conductive materials. This is because conductive materials have free charges that will move to form a field opposite to that impinged upon it. This leads to an exponential decay of the magnitude of the field with depth [14]. The performance of GPR is thus degraded in the presence of moisture; either from water on the surface or within the pores of the material. The attenuation increases with frequency, so lower frequencies can be used, but this inevitable leads to a reduction in the spatial resolution of the method. This is a sever limitation and one fundamental to the method. For example consider the use of a 1 GHz (and thus a wavelength of 30 cm, giving a mediocre spatial resolution) electromagnetic wave incident upon wet clay. The attenuation in this case is over 100 dBm^{-1} [11], making it very difficult to detect reflections from targets at any notable depth.

Field experiments have been performed with good rates of detection, although the false alarm rate is still reasonably high [1]. However testing with positive results does not mean that the same results can be obtained in soils with higher conductivities or those with inhomogeneities present. For GPR recent rainfall may be enough to prove the method ineffectual. This does not mean that it is not however useful. It's most likely implementation is in conjunction with other technologies such as metal detectors [15].

1.1.3 - Other Methods

Whilst electromagnetic induction and ground penetrating radar are the two most developed technologies many other techniques have been investigated and examined for shallow buried object detection. Landmine detection in particular has recently received a large amount of interest and several specific technologies have been developed for this purpose. These rely on the detection of the explosive material within the landmine in order to locate the target.

One example is the technique of nuclear quadrupole resonance NQR [16]. This method examines the difference in the nuclear energy levels formed by the splitting of degenerate nuclear states by electrostatic interaction of the nucleus with the surrounding electrons. Due to the degree of energy level splitting the frequencies radiated after excitation of the nucleus provide a distinct signature of the compound. As the method can be used to detect specific explosive compounds, clutter objects which can confound over methods, such as large amounts of magnetic clutter or inhomogeneous ground properties, are undetectable using NQR. The disadvantage of the method locating specific compounds rather than mines directly is that leakage of

the explosive compounds or contamination from exploded mines will cause false detections.

Perhaps surprising is the reliance of demining teams on very basic methods. A simple prodding stick is still a mainstay of demining [17] and is simply carefully pushed into the ground ahead of the user to feel for any buried objects. The use of dogs, and more recently trained rats [1, 18] is still commonplace. Whilst these methods seem primitive, the fact that they are still in widespread usage indicates the limitations of the current level of technology.

Passive electromagnetic methods of detection, such as microwave radiometers, also exist [19]. These detect both the low intensity reflections from incident radiation and the emitted thermal radiation from buried objects whose temperature is likely to vary slightly in comparison with the surrounding background. These have very short interrogation depths of just a few centimetres due to the same physical constraints as all electromagnetic methods. Furthermore passive electromagnetic methods will be as susceptible to attenuation in conductive media as the active methods.

1.2 - Seismic Methods

1.2.1 - Surface Wave Methods

The majority of work on surface wave detection methods has been undertaken at two research institutes working independently of each other; the Georgia Institute of Technology [20-22] and the University of Mississippi [23-25]. Whilst there are significant differences in implementation, the common physical principles behind detection and the associated advantages and limitations are shared, and shall be consider first before analysis of the individual methods.

Surface waves are induced which cause excitation of the target. The motion of the ground above the target is measured with larger motion assumed to correspond to the location of a target. The motion of the ground above the target will be maximal if the target possesses structural resonances and the input excitation has significant amounts of energy at these frequencies. As this method relies on the resonances of the target to generate large enough surface displacements for detection it is relatively immune to clutter. Metallic clutter such as shrapnel that produces false alarms with metal detectors and natural inhomogeneities such as tree roots and rocks that produce false alarms in GPR lack the resonances required for detection with this method. Furthermore by examining the excitation frequencies that lead to maximal response the information on the values of the structural resonances of the target could be deduced, leading to more accurate target discrimination between compliant objects.

There are two limitations of the general principle which restricts the application of the method. The first of these is that if the target is not buried close to the surface then, even when structural resonances are excited, the surface motion of the ground will be too small for detection. The depth at which targets can no longer be detected will depend on a large number of factors and separate consideration will be given for each of the two methods. This limitation, coupled with the need for structural resonances of the target, means that this method specifically lends itself to the detection of buried antipersonnel landmines. These have been experimentally shown to possess the

required structural resonances [26, 27], and are in general buried at sufficiently shallow depths for the method to be practical.

The second of these limitations is that the method has zero stand off; it mandates measurement directly above the target. This is particularly problematic for application to landmine detection where it is obviously desirable for no force to be applied directly above the target in order to minimise the chances of detonation. As the method has no ranged detection ability the measurement of the surface must be taken over every part of the ground where a target may exist. This limits the operational speed of the method.

The method developed by the Georgia Institute of Technology [22] uses an electrodynamic shaker as the excitation source. This is used to excite Rayleigh surface waves which propagate to the target and cause excitation. The velocity profile of the ground is then measured using an electromagnetic radar system with regions of high velocity assumed to correspond to the location of the target. The use of Rayleigh waves has the advantage that as they are surfaces waves they suffer less from geometric spreading than body waves, meaning that the more energy should reach the target. The amplitude of the Rayleigh wave vibrations however fall off quickly with depth [28], with increasing reduction with increasing depth. This presents a further constraint on the depth to which the method may be used.

Experimental work undertaken in the laboratory using the method and has shown that it is capable of detecting shallow buried landmines [21], even when closely spaced. The experimental work has however been undertaken in scenarios too contrived to assume that measurement reliability is transferable to real world applications. The use of electromagnetic radar in order to measure ground movement furthermore prohibits the use of the method when surface coverings are opaque to the electromagnetic radiation used, for example in the presence of surface water or in moist soils.

Work has continued on the method by examining the possibility of using contact rather than non-contact sensors in order to overcome these problems [20], as well as reduce costs. Standard seismic geophones are not feasible as their insertion into the ground directly above the target may result in detonation. This research demonstrated that contact accelerometers could be used safely provided adequate care was taken not to exert too great a force on the ground, enabling the use of closely spaced arrays. However it is questionable how applicable the laboratory setup would be in practical situations with uneven ground. A further problem is that the operational speed of the device is limited compared to the non-contacting method, where the ground could be scanned using a synthetic array.

The method developed by researchers at the University of Mississippi uses acoustic-to-seismic excitation where an acoustic source is located above the ground and used to induce seismic vibrations [23]. This method was first considered in the early seventies [29] for detecting buried objects. More detailed examination of the technique was performed by the University of Mississippi researchers, confirming the acoustic-to-seismic method to be a theoretically and experimentally viable [24, 25] method of transferring energy into the ground.

This may initially appear counter intuitive as the large impedance discontinuity between the air and the ground can be expected to reflect most of the acoustic energy impinged upon it. However provided the soil is porous the input impedance to the ground will be far lower than might be assumed for a body of homogeneous material. Physically this can be attributed to acoustic waves propagating into the pores of the material, a theory first established mathematically by Biot [30]. The transfer of energy from the pore wave propagation to seismic vibrations via viscous drag results in a significant lowering of the ground impedance. The transmission coefficient, even taking this extra coupling into account, remains low, at around 1%.

Acoustic-to-seismic excitation has the advantage that it does not require contact with the ground, allowing for the possibility of attachment to a moving vehicle. Furthermore as the Biot waves propagating in the ground have a lower velocity than those in air the sound will be refracted towards the vertical plane [31]. This means that an acoustic source need not be located directly above the target to achieve adequate illumination.

The method developed measures the response of the buried target using a laser Doppler vibrometer (LDV). An LDV consists of laser shone onto the ground with the reflection from the surface measured by heterodyning with a reference signal. This enables one to obtain the velocity value at the ground surface by finding the small difference between the outputted signal frequency and the Doppler shifted return signal [32]. Little post-processing is performed; the high regions of velocity are simply assumed to be a target. The use of an LDV had the advantage of being non-contact but eliminates the standoff desired for detection.

When used in conjunction with acoustic-to-seismic excitation a problem is presented; the high sound pressure levels required to transmit enough energy through the air-soil interface, over 110 dB [33], can couple with the LDV. Movement of the LDV relative to the soil will cause the LDV's ability to measure the surface velocity to suffer. Difficulties in stabilising the LDV have been reported [32], and although they have been overcome in field testing to date these could cause serious issues in difficult field conditions.

Field results to date have proved promising. The method has been able to detect landmines in field experiments, even when closely spaced. The methods ability to distinguish from clutter in field experiments reported in [33] is however not ideal. In order to differentiate a target mine from natural clutter the velocity profiles had to be analysed over a frequency range in order to identify anti-resonances as well as resonances in the velocity profile. If the method relies on this level of post processing then it is unlikely that an automatic detection system could be successfully implemented.

The false alarm rate is further increased when there are strong variations in the natural properties of the ground (such as density). These result in a complex acoustic-to-seismic transfer function leading to regions of high relative velocity despite the absence of a target. The effect of these variations has been documented both theoretically and experimental [34].

The depth limitations of the method have not been thoroughly analysed by the methods developers. This is likely to be because the method has been designed only with consideration to landmines buried at shallow depths. The depth limitations will be caused by the same two effects as in the Georgia Institute of Technology method; rapidly reducing amplitude of input excitation with depth and an inability for targets buried at depth to produce adequate surface motion for measurement. The former of these is, unlike in the previous cases of Rayleigh wave decay with depth, likely to vary widely with specific ground properties. For example if the ground is water saturated the acoustic-to-seismic coupling can be expected to be very poor, leading to little target excitation and thus reduced probability of detection. This restriction is particularly problematic given that any new detection method should ideally complement the existing technologies of metal detectors and GPR, rather than suffer from similar environmental limitations.

1.2.2 - Seismic Excitation & Detection

Research has been undertaken into the use of methods using both seismic excitation and measurement. In these a signal is generated by contact with the ground; excited waves then propagate and are reflected off the target and measured by contact transducers. The time between emission and reception of the signal can be used to give an indication of the distance to the target, providing the wavespeed in the medium is known. This method has the ability for a notable standoff, with the limiting factor likely to be the reduction in signal intensity due to both geometric spreading and ground attenuation

The method of seismic excitation has several advantages over acoustic-to-seismic methods previously discussed. There is no reliance on the soil to be porous, as required for acoustic-to-seismic coupling. The method is therefore equally applicable to dry and saturated soils. The use of seismic excitation over acoustic methods also enables for the specific excitation of bulk waves (compressive and/ or shear) as well as surface Rayleigh waves as there is direct control over the interaction on the ground. All three main types of seismic waves (compressional, shear and Rayleigh) have been evaluated individually [35] with the choice of wave depending mainly on the depth of target.

Laboratory experiments have been undertaken in order to assess the validity of the method [36]. Attempts were made to measure both a shallow and deep target using all three types of waves individually in a large sand tank. Detection abilities were poor for two reasons. The first is that the attenuation of the seismic signal is frequency dependant, with higher frequency vibrations suffering from significantly higher attenuation than lower frequencies. This results in a lower bandwidth of measured signal, increasing side lobes in the autocorrelation function [37] used to analyse the data and obscuring low intensity reflected signals. A possible solution used to overcome this problem is to increase the magnitude of the input signal as a function of frequency in order to at least partially compensate for ground attenuation [38].

The second problem is that the return signal is contaminated by reflections and reverberation from the boundaries of the tank, resulting in partial correlation at many time intervals. This effect is, in laboratory experimentation considering the frequency domain, if anything, beneficial. This is because the reflected/ reverberant energy will excite the target above levels achieved in conditions with no boundaries (i.e. in the

field). Attempts can be made to provide anechoic terminations at the surface boundaries to suppress standing surface waves, but this has caused little improvement in documented experiments. Experimentation in the field, although introducing a lack of control into the measurements, would ensure that reverberation energy is severely reduced.

A different approach has been undertaken by researchers at the University of Yokohama with the aim of imaging for archaeological purposes [39-43]. For this method a line array of sensors is used and a cross-sectional image through the ground is formed. This is achieved by calculating the time of flight of the disturbance to each sensor for each possible location of the target and then summing the appropriate contributions from the time domain measurements. This is similar to the established common depth point stack (CDPS) method in deep subsurface investigations for hydrocarbon reserves [44].

The method specifically uses shear waves in order to maximise the time interval between the Rayleigh wave and reflected shear wave, thus preventing the smaller reflected signal from being obscured by the dominant surface wave. This method has been field tested to produce acceptable results with suitable post processing. As only impulsive sources were used it is possible that more complex excitation signals could improve the method.

Underlying all the above methods is a fundamental flaw; the reflection method as implemented above can give information only about the presence and approximate dimensions of a target but not on its nature. Further techniques must be developed if these methods are to be used in situations where many objects other than the intended target are likely to be present. The advantageous feature of non-zero standoff may also be compromised by high ground attenuation, values of which are often difficult to obtain in the literature.

1.2.3 - Non-Linear Techniques

A new method has recently been developed by Donskoy [26] based on non-linearities introduced by compliance of the target. For compliant objects above resonance the target surface and the surrounding soil will move out of phase with each other, causing them to separate. This causes a non-linear change in stiffness in the oscillation as the separation will only occur in the tensile part of the vibration. This is achieved even for reasonably low levels of excitation. Clutter items, such as rocks, typically have resonances well outside of the frequency range of excitation. As such the surface of the object will move in phase with the adjacent soil and linear transmission of the vibration can occur. Thus clutter discrimination is reliably achieved.

When a non-linear system is excited simultaneously with two sinusoids of different frequencies sum and difference tones are produced. This has been experimentally and theoretically verified for land mines [45, 46]. Thus a system featuring a relatively compliant target can be excited with two frequencies and a one or more other predictable frequencies can be measured to indicate the presence of the target. This has the advantage that the output signal can band pass filtered to remove the relatively large input to the system.

Field tests have been performed and the non-linear physics has been analysed using lumped parameter models, both indicating the validity of the method. Clutter rejection is, as expected, excellent. As yet the method has been applied only using acoustic-to-seismic coupling and LDV to measure surface displacement. As such, the flaws associated with these methods are also present.

1.3 - Technologies from Other Media

Although this work shall be concerned with detection and localisation of objects buried in the ground, analogous problems in other media have been the subject of much investigation. Sonar refers to the detection (and in the case of active sonar emission) of underwater acoustic waves with the aim of target location and identification. Because the waves propagate in water, which cannot support shear forces, there is only compressional wave propagation eliminating the problem of interaction of multiple wave types with a target. Sonar is an established technology and complex post-processing methods have been already been developed [47]. As many sonar techniques use the same sensor arrangement (a uniform line array) as the seismic method to be used, there is the possibility of modifying the existing sonar post-processing techniques for application to the shallow seismic detection problem.

One very commonly employed method is that of beamforming [48, 49]. This exploits the directivity of a line array of omnidirectional sensors. Summing the outputs of the sensors of the array gives, in a given frequency range, a single direction in which the array is particularly sensitive. By introducing time delays and amplitude weightings to the sensor outputs prior to their summation both the direction of the main beam can be altered and the sensitivity of the array to energy from direction away from the look direction minimised. Directions containing large amounts of energy are assumed to correspond to target locations.

The standard method of beamforming cannot be used directly as it relies on the assumption of the energy source lying in the far-field, which will not be valid for shallow seismic localisation. Standard beamforming also fails to provide information as to the range of the target, preventing accurate localisation of the target without triangulation via several measurements from different locations. These problems may be overcome by the use of nearfield beamforming [50].

Active sonar uses an excitation source to induce acoustic waves that propagate to the target and are reflected. Active methods make use of correlation functions in order to calculate relative time delays between time extended signals [48], a method likely to be applicable to active seismic detection techniques. The correlation functions enable more advanced post-processing methods, such as MUSIC (multiple signal classification) [51]. This method exploits the orthogonality of the eigenvectors of a matrix of correlation functions between sensor outputs to isolate the target signal from noise.

Similar methods to those used in the seismic work of Sugimoto et. al. [42] are used in the area of non-destructive testing [52, 53]. For non-destructive testing the aim is to localise anomalies in structures that could represent faults. These methods tend to employ very short input pulses and thus much higher frequencies, on the order of hundreds of thousands of Hertz. Propagation of these frequencies is possible in the

materials under test, such as concrete, but would not be possible in soil without very rapid attenuation.

Radar refers to target location in air. For this purpose electromagnetic rather than acoustic waves are used, and as such the physical principles of the propagation have little applicability to the problem of seismic detection. There are many similarities in the signal processing techniques used in sonar [54]. Some of these may be immediately overlooked, such as the use of Doppler shifts to give information on target velocity. This is obviously not applicable to targets buried underground.

Section 2 - Background Theory

The theory of elasticity is well established and documented [55, 56] and a brief summary of the basic theory given in Appendix A. This section contains application of this basic theory to the problem of wave propagation in elastic media. This is necessary for understanding and interpreting the behaviour of the waves used to attempt to locate buried objects.

2.1 - Infinite Elastic Space

The simplest mathematical application of the basic equation of elasticity to three-dimensional spaces is that of the infinite elastic space, as it features no boundaries for disturbances in the medium to interact with. The derivation of the general equation of motion and its subsequent solutions are given in this section.

2.1.1 - Derivation of the General Equation of Motion

Consider an element of a infinite elastic medium in a general Cartesian space with dimensions $\delta x_i \times \delta x_j \times \delta x_k$. The element is shown in Figure 2.1 with only stresses acting in the x_i direction. Applying Newton's second law in order to relate the forces in the x_i direction and the subsequent displacement yields

$$\left(\sigma_i + \frac{\partial \sigma_i}{\partial x_i}\delta x_i\right)\delta x_j \delta x_k - \sigma_i \delta x_j \delta x_k + \left(\tau_{ij} + \frac{\partial \tau_{ij}}{\partial x_j}\delta x_j\right)\delta x_i \delta x_k - \tau_{ij}\delta x_i \delta x_k + \left(\tau_{ik} + \frac{\partial \tau_{ik}}{\partial x_k}\delta x_k\right)\delta x_i \delta x_j - \tau_{ik}\delta x_i \delta x_j = \rho \delta x_i \delta x_j \delta x_k \frac{\partial^2 u_i}{\partial t^2}, \tag{2.1}$$

where ρ denotes the density of the material and all other quantities are defined in Appendix A. Equation 2.1 simplifies to

$$\frac{\partial \sigma_i}{\partial x_i} + \frac{\partial \tau_{ij}}{\partial x_j} + \frac{\partial \tau_{ik}}{\partial x_k} = \rho \frac{\partial^2 u_i}{\partial t^2}. \tag{2.2}$$

Substitution of Equations A.2, A.6 and A.8 from Appendix A into Equation 2.2 and simplifying gives

$$(\mu + G)\frac{\partial}{\partial x_i}(\nabla \bullet \mathbf{u}) + G\nabla^2 u_i = \rho \frac{\partial^2 u_i}{\partial t^2}, \tag{2.3}$$

where ∇ denotes dell, a spatial partial derivative operator defined by $\nabla = \frac{\partial}{\partial x_i}\hat{\boldsymbol{x}}_i + \frac{\partial}{\partial x_j}\hat{\boldsymbol{x}}_j + \frac{\partial}{\partial x_k}\hat{\boldsymbol{x}}_k$. Summing the three equations described by Equation 2.3 and expressing in terms of only the displacement vector $\mathbf{u}$ gives a final general equation describing the system;

$$(\mu + G)\left[\nabla(\nabla \bullet \mathbf{u})\right] + G\nabla^2 \mathbf{u} = \rho \frac{\partial^2 \mathbf{u}}{\partial t^2}. \tag{2.4}$$

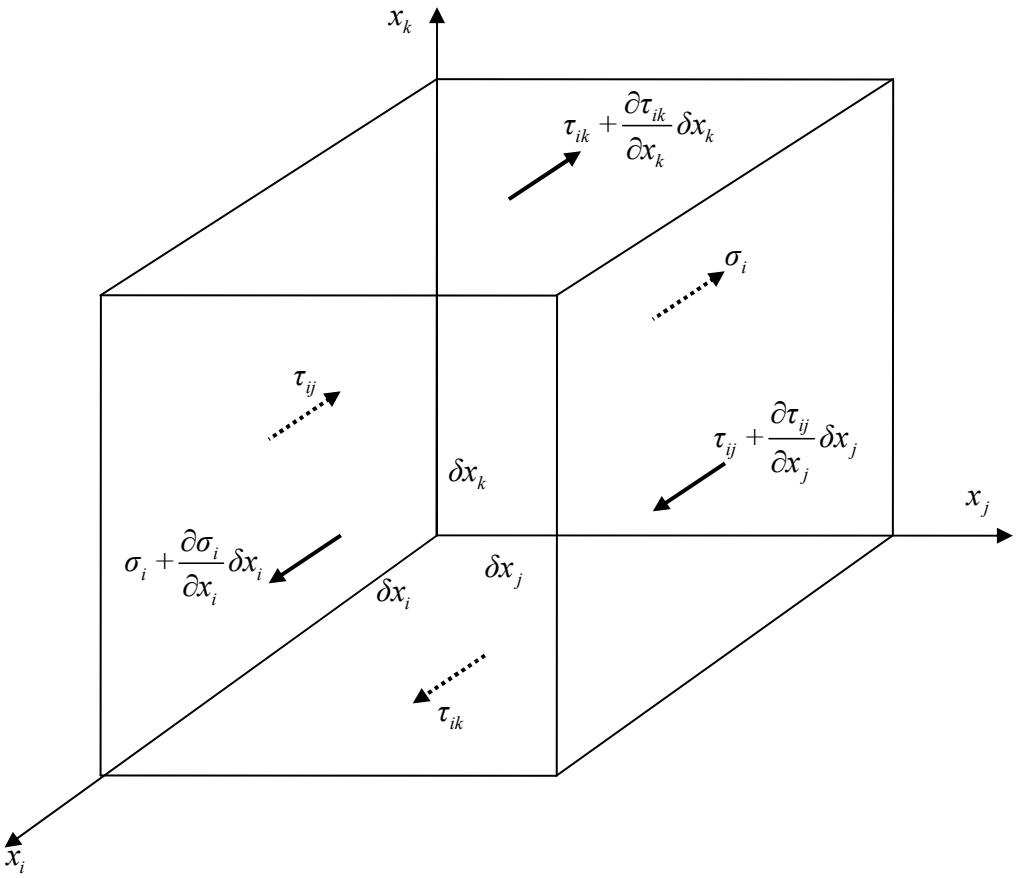

Figure 2.1 - Diagram of an element of an infinite elastic space showing stresses acting in the x_i direction. The element has dimensions $\delta x_i \times \delta x_j \times \delta x_k$. Dashed arrows show stresses from the rear sides of the element.

2.1.2 - Compressional wave propagation

Taking the divergence of both sides of Equation 2.4 gives an expression with the form of a wave equation in terms of the divergence of the displacement vector, which is denoted by ε:

$$\nabla^2 \varepsilon = \frac{1}{c_c{}^2} \frac{\partial^2 \varepsilon}{\partial t^2}, \tag{2.5}$$

where $c_c = \sqrt{(\mu + 2G)/\rho}$ and $\varepsilon = \nabla \bullet \mathbf{u}$. This implies that the medium is capable of supporting propagations in variations in the quantity ε. The physical significance of this quantity can be found by considering a volume element of a generic space whose dimensions $x \times y \times z$ are infinitesimally expanded to become $(x + \delta x) \times (y + \delta y) \times (z + \delta z)$. Neglecting second order small terms, the ratio of the change in volume to the original volume is given by a summation of the axial strains:

$$\frac{\delta V}{V} = \frac{\delta x}{x} + \frac{\delta y}{y} + \frac{\delta z}{z} \tag{2.6}$$

As ε is the sum of the axial strains, Equation 2.5 can be physically interpreted to mean that an infinite elastic space supports the propagation of waves of compression with a wavespeed c_c. It should be noted that the wave propagation is non-dispersive and is a function only of the Young's modulus, the Poisson's ratio and the density of the material.

2.1.3 - Shear Wave Propagation

Taking the curl of both sides of Equation 2.4 and using the fact that the curl of a gradient is always zero gives an expression with the form of a wave equation in terms of the vector $\boldsymbol{\Omega}$:

$$\nabla^2 \boldsymbol{\Omega} = \frac{1}{c_s^{\,2}} \frac{\partial^2 \boldsymbol{\Omega}}{\partial t^2}, \tag{2.7}$$

where $c_s = \sqrt{G/\rho}$ and the vector $\boldsymbol{\Omega}$ is defined by $2\boldsymbol{\Omega} = \nabla \times \mathbf{u}$. A physical interpretation of this result can be found by considering the pure rotation of a two dimensional element of the space about the x_k, as shown in Figure 2.2. The angle of rotation can, by geometric considerations, be seen to be

$$\Omega_k = \frac{\partial u_j}{\partial x_i}, \qquad \Omega_k = -\frac{\partial u_i}{\partial x_j}. \tag{2.8}$$

The sum of the expressions in Equation 2.8 gives the rotation about a single axis to be

$$2\Omega_k = \left(\frac{\partial u_j}{\partial x_i} - \frac{\partial u_i}{\partial x_j} \right) \hat{\boldsymbol{x}}_{\boldsymbol{k}}. \tag{2.9}$$

The vector $\boldsymbol{\Omega}$ is defined as the sum of the rotations about all three axes. Thus

$$2\boldsymbol{\Omega} = \left(\frac{\partial u_k}{\partial x_j} - \frac{\partial u_j}{\partial x_k} \right) \hat{\boldsymbol{x}}_{\boldsymbol{i}} + \left(\frac{\partial u_i}{\partial x_k} - \frac{\partial u_k}{\partial x_i} \right) \hat{\boldsymbol{x}}_{\boldsymbol{j}} + \left(\frac{\partial u_j}{\partial x_i} - \frac{\partial u_i}{\partial x_j} \right) \hat{\boldsymbol{x}}_{\boldsymbol{k}}$$

$$\Rightarrow 2\boldsymbol{\Omega} = \nabla \times \mathbf{u}. \tag{2.10}$$

The wave equation in $\boldsymbol{\Omega}$ given by Equation 2.7 can therefore be physically interpreted an infinite elastic space supporting the propagation of waves of rotation of the medium. The wavespeed of these propagations is denoted c_s, and the type of wave propagation referred to as a shear wave. The wavespeed is again non-dispersive and only a function only of the Young's modulus, Poisson's ratio and density of the material. Under deformation of the element the angle of rotation will not be equal from both axes in the plane of consideration, as shown in Figure 2.2. In these circumstances the angle obtained from Equation 2.9 can be considered to be an average of the two physical angles [56] and the derived equation maintains its validity.

Using the relation between the elastic constants given by Equations A.7 and A.8 the ratio of the two wavespeeds can be expressed in terms of only the Poisson's ratio;

$$\frac{c_c}{c_s} = \sqrt{\frac{2(1-v)}{1-2v}}\,. \tag{2.11}$$

As the Poisson's ratio will always be in the range $0 < v < 0.5$ the compressional wavespeed will always exceed the shear wavespeed by at least a factor of the square root of two.

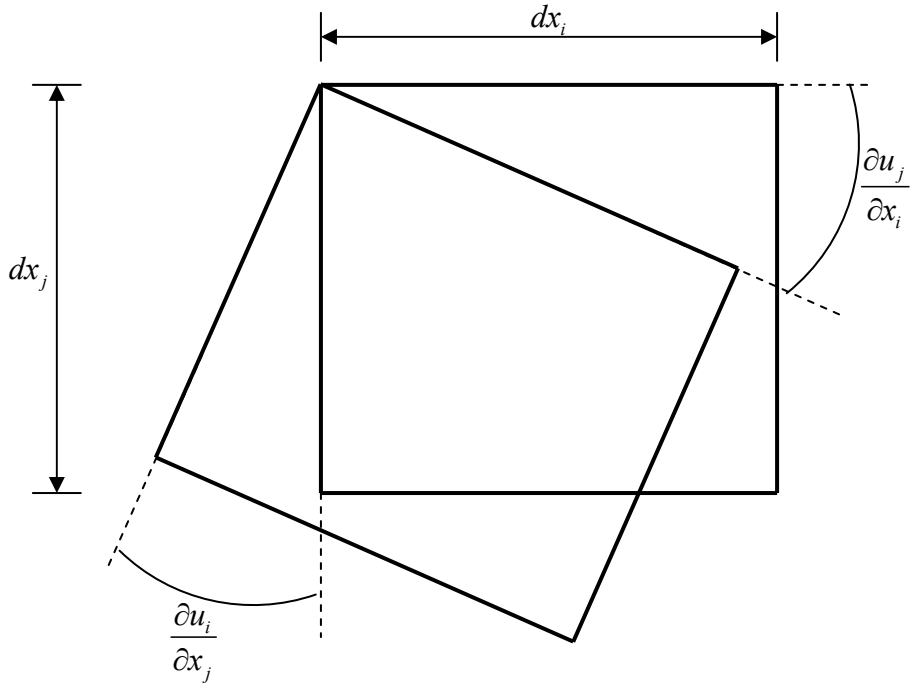

Figure 2.2 - Diagram of rotation of a $\delta \boldsymbol{x}_i \times \delta \boldsymbol{x}_j$ element showing relevant angles.

2.1.4 - Plane wave propagation

In order to investigate wave propagation in an infinite elastic space it is useful to examine plane wave propagation. A general plane wave is described by

$$\mathbf{u} = \mathbf{A} f\left(\mathbf{n} \bullet \boldsymbol{x} - ct\right). \tag{2.12}$$

where **u** denotes the displacement vector, **A** vector of amplitudes of the waveform, **n** a unit vector in the space normal to the plane waveform defining the direction of propagation, $\boldsymbol{x}$ a position vector in the space and f an arbitrary function describing the waveform. This can be substituted into the equation of motion of the system given by Equation 2.4. The resultant expression is given by [57]

$$\left(\mu + G\right)\left(\mathbf{A} \bullet \mathbf{n}\right)\mathbf{n}_i + GA_i = \rho c^2 A_i \tag{2.13}$$

In order to simplify the result the assumption is made that the wave propagates

parallel to the z direction. As an infinite isotropic elastic space is considered this causes no loss of generality. Equation 2.13 thus reduces to

$$\left(\mu + G\right)\mathbf{A}_z\left(\mathbf{n}_z \bullet \mathbf{n}_i\right) + \left(G - \rho c^2\right) = 0\,. \tag{2.14}$$

As the components of the normal vector are orthogonal, $\mathbf{n}_i \bullet \mathbf{n}_j = \delta_{ij}$, where δ_{ij} is the Kronecker delta. Consider the case of wave displacement in the x direction (i.e. perpendicular to the direction of wave propagation). Setting $i = x$ gives the wavespeed to be

$$c_x = \sqrt{\frac{G}{\rho}} = c_s\,, \tag{2.15}$$

where the wavespeed is as the shear wave speed given by Equation 2.7. Considering $i = y$ an identical result is obtained. As such it can be seen that the shear waves are transverse and can be decomposed into two mutually orthogonal components. These are generally referred to in the literature as shear vertical (SV) and shear horizontal (SH) waves, although in an infinite isotropic space the decomposition is arbitrary due to the system symmetry.

The final case of $i = z$ describes particle motion in a direction parallel to the direction of wave propagation and therefore represents a longitudinal wave. Substitution into Equation 2.14 gives the unsurprising result that

$$c_z = \sqrt{\frac{\mu + 2G}{\rho}} = c_c \tag{2.16}$$

which is the compressional wavespeed.

It should be noted that any assumption of plane wave propagation in the near-field considered in shallow seismic excitation will be invalid. For localised sources used for excitation in the proceeding work plane wave propagation will only become a valid approximation of spherical wave propagation in the far-field. Nevertheless the concepts of plane wave propagation are useful in developing an understanding of the system.

2.2 - Rayleigh Waves

In this section the infinite elastic space considered in the Section 2.1 is modified by the introduction of a free boundary. For convenience let the free boundary be in the *x*-*y* plane with the origin of the *z* axis defined at this boundary, and with a positive *z* direction corresponding to increasing distance from the free surface. The equations describing the infinite elastic space are given by Equations 2.4. The displacement vector **u** can be split into two potentials as follows;

$$\mathbf{u} = \nabla\xi + \nabla\times\boldsymbol{\psi}, \qquad \nabla\bullet\boldsymbol{\psi} = 0\,, \tag{2.17a,b}$$

where ξ is a scalar potential and a $\boldsymbol{\psi}$ vector potential. Note that although this is a general mathematical theorem these potentials have particular physical significance in this application. These two potentials correspond to the compressional and rotational parts of the motion respectively. Equation 2.17 can thus be viewed as a statement that the motion of the medium is the superposition of compressional and rotational motions. Substitution of the potential form of the displacement into the equation of motion of the system given by Equation 2.4 gives

$$\nabla\left[\left(\mu+2G\right)\nabla^2\xi - \rho\frac{\partial^2\xi}{\partial t^2}\right] + \nabla\times\left[G\nabla^2\boldsymbol{\psi} - \rho\frac{\partial^2\boldsymbol{\psi}}{\partial t^2}\right] = 0\,. \tag{2.18}$$

As the terms in square brackets must equal zero two wave equations can be obtained, one for each potential:

$$\nabla\xi = \frac{1}{c_c}\frac{\partial^2\xi}{\partial t^2}, \qquad \nabla\boldsymbol{\psi} = \frac{1}{c_s}\frac{\partial^2\boldsymbol{\psi}}{\partial t^2}\,. \tag{2.19a,b}$$

These have wavespeeds corresponding to the compressional and shear waves, which is unsurprising considering these potentials correspond to these separate components of the motion.

The case of wave propagation in the *x* direction can be taken without loss of generality due to the symmetry of the system. The motion will therefore have no dependence on the *y* direction. As such the displacement variables in the *x* and *z* directions immediately reduce to

$$u = \frac{\partial\xi}{\partial x} + \frac{\partial\psi}{\partial z}, \qquad w = \frac{\partial\xi}{\partial z} - \frac{\partial\psi}{\partial x}\,. \tag{2.20a,b}$$

Solutions to Equations 2.19a,b are assumed harmonic with general depth dependence. Denoting the depth dependence by $F(z)$ and $G(z)$ for the potentials gives solutions of

$$\xi = F(z)e^{j(kx-\omega t)},$$

$$\psi = G(z)e^{j(kx-\omega t)}, \tag{2.21}$$

where k denotes the wavenumber and ω the angular frequency. As we are dealing with motion in one plane the rotation vector potential reduces to a scalar. Taking the potential ξ and substituting into the appropriate wave equation of Equation 2.19 gives a differential equation describing the depth dependency:

$$\frac{d^2F(z)}{dz^2} = q^2F(z), \qquad q^2 \equiv \left(k^2 - \eta_1\right), \qquad \eta_1 \equiv \frac{\omega^2}{c_c^2}. \tag{2.22}$$

The two constants have been defined for later convenience. This has the general solution of

$$F(z) = Ae^{-qz} + Ce^{qz}. \tag{2.23}$$

The latter term of this equation can be disregarded as q must always be positive and exponential growth of the motion with increasing depth is not physical. A similar procedure can be undertaken to obtain the expression for the depth dependency of the ψ potential, giving the result that

$$G(z) = Be^{-sz}, \qquad s^2 \equiv \left(k^2 - \eta_2\right), \qquad \eta_2 \equiv \frac{\omega^2}{c_s^2}. \tag{2.24}$$

The two potentials are therefore given by

$$\xi = Ae^{-qz+j(kx-\omega t)},$$

$$\psi = Be^{-sz+j(kx-\omega t)}. \tag{2.25}$$

In order to continue it is necessary to introduce boundary conditions. As the free surface can produce no forces to oppose the motion the stresses on the surface must be zero. Thus

$$\sigma_z = \tau_{zx} = 0. \tag{2.26}$$

The expression for the normal stress is given in Equation A.1. This can then be expressed in terms of potential functions using Equations 2.20, where the potentials must be evaluated at $z = 0$ as the constraint is being applied at the free surface:

$$\sigma_z = (\mu + 2G)\left.\frac{\partial^2\xi}{\partial z^2}\right|_{z=0} + \mu\left.\frac{\partial^2\xi}{\partial x^2}\right|_{z=0} - 2G\left.\frac{\partial^2\psi}{\partial x\partial z}\right|_{z=0} = 0. \tag{2.27}$$

Using Equations 2.21 evaluated at $z = 0$ the ratio of the two constants associated with the decay of the motion can be obtained as

$$\frac{A}{B} = \frac{2jGsk}{(\mu + 2G)q^2 - \mu k^2}. \tag{2.28}$$

The shear stress is described by Equations A.2 and A.6. A similar process can be used to first obtain the constraint in terms of the potential as

$$2\frac{\partial^2\xi}{\partial x\partial z}\bigg|_{z=0} - \frac{\partial^2\psi}{\partial x^2}\bigg|_{z=0} + \frac{\partial^2\psi}{\partial z^2}\bigg|_{z=0} = 0\,, \tag{2.29}$$

and then obtain another ratio of the two constants associated with the vertically reducing amplitude;

$$\frac{A}{B} = \frac{k^2 + s^2}{2jqk}\,. \tag{2.30}$$

Equating these two ratios enables one to obtain a cubic equation in terms of the quantity $\eta^2 = \left(\eta_2/k\right)^2$;

$$\eta^6 - 8\eta^4 + 8\left(3 - 2\alpha^2\right)\eta^2 - 16\left(1 - \alpha^2\right) = 0\,, \tag{2.31}$$

where α is the ratio of the shear to compressional velocities in the medium and is governed only by the Poisson's ratio of the material. The significance of the quantity η can be found by substituting the definition of η_2 from Equation 2.24. As the ratio of the angular frequency to wavenumber in the material is the speed of propagation of the wave, which is denoted by c_R;

$$\eta = \frac{\omega}{c_s}.\frac{1}{k} = \frac{c_R}{c_s}\,, \tag{2.32}$$

and η is therefore the ratio of the surface wavespeed to the shear wavespeed. This type of wave propagation is named a Rayleigh wave after the first man to study them in detail [58]. As none of the quantities in Equation 2.31 are frequency dependent the Rayleigh wave propagates without dispersion.

As the functions describing the depth dependency of the motion of the medium are exponentials the coefficient of the depth variable in their argument must be negative to prevent the unphysical situation of infinite motion infinitely far from a disturbance. In order for this to be the case both *q* and *s* must be non-negative. From Equation 2.22 and 2.24 this gives the constraints

$$\frac{c_r}{c_s} < 1, \qquad \frac{c_r}{c_c} < 1\,. \tag{2.33a,b}$$

The Rayliegh wave must always propagate slower than the compressional and shear waves. Equation 2.31 can be solved numerically to give the ratio of the Rayleigh to shear wavespeeds as a function of the Poisson's ratio. Over the possible range of values for the Poisson's ratio the ratio of the wavespeeds varies between about 0.88 and 0.96 [57]. The Rayleigh wave is thus constrained to propagate at a speed slightly less than the shear wavespeed.

The displacement of the Rayliegh wave components can be found by substituting the expressions for the potentials into the expression relating the displacement and potentials given by Equation 2.20. One of the arbitrary constants of Equation 2.25 can then be eliminated using Equation 2.30. After simplification the horizontal and vertical displacements are found to vary with the product of the wavenumber and depth as;

$$U\left(kz\right) = e^{-q'kz} - \frac{2s'q'}{1+s'^2} e^{-s'kz},$$

$$W\left(kz\right) = \frac{2q'}{1+s'^2} e^{-s'kz} - q'e^{-q'kz}, \tag{2.34}$$

where

$$q' = \sqrt{1-\alpha^2\eta^2}, \quad and \quad s' = \sqrt{1-\eta^2}\ .$$

These functions vary only with the Poisson's ratio of the material, and are plotted in Figure 2.3 for the specific case of $v = 0.45$. It can be seen that the displacement quickly falls off with increasing depth, and that the reduction in wave amplitude will be higher for higher frequencies. For depths over about three times the wavelength the displacements are negligible; of order of half of one percent of the surface amplitude. The direction of the horizontal displacement can be seen to reverse at a depth of about one fifth of a wavelength.

In general the ground will be a layered media due to sedimentary structure. The stiffness of these layers is likely to increase with increasing depth. As longer wavelengths penetrate deeper into the ground they will propagate, on average, in stiffer media and because of this propagate faster. Despite the theoretically non-dispersive nature of Rayliegh waves, in practice they will therefore exhibit dispersive behaviour. This behaviour will be prominent once the wavelength becomes of the same order as the distance between geological layers.

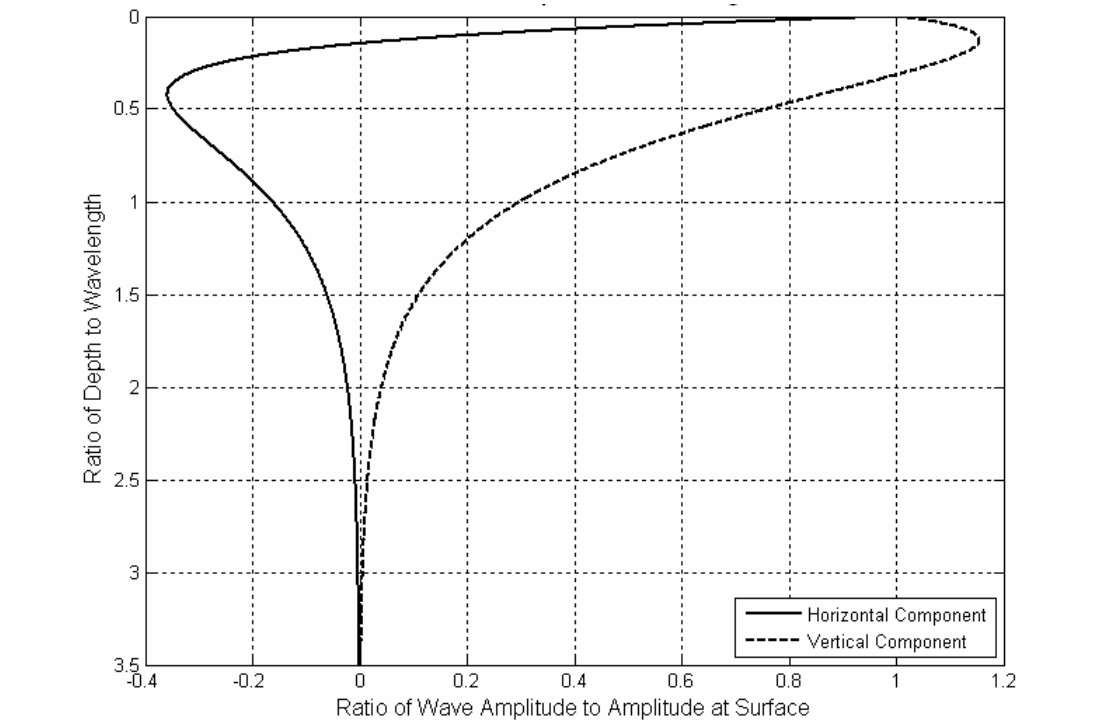

Figure 2.3 - Plot of the horizontal and vertical displacements of a Rayleigh wave as a function of the dimensionless ratio of the depth *z* to the wavelength λ, with $v = 0.45$. Displacements are normalised to the surface amplitude. Note that in order to calculate the wavespeed ratios required for implementation both Equation 2.11 and the approximate relation that $\frac{c_R}{c_s} = \frac{(0.87 + 1.12v)}{(1+v)}$ obtained from [57].

Section 3 - Time Domain Stacking

Time domain stacking is an existing method developed by Sugimoto et. al. [42] for underground target localisation. In this section the method is described and its limitations discussed.

3.1 - Wave Reflections & Selection of Wave Type

In order to search for the location of objects buried in the ground, wave reflections may be used. A disturbance can be created on the surface of the ground which will propagate to the target and be reflected. This reflection can then be measured on the surface of the ground. Given the speed of wave propagation in the material the time delay between the emission and reception of the signal at the surface can be used to obtain an estimate of the distance to the target. This method is used analogously in other technologies such as radar.

Complications are introduced by the fact that multiple types of waves will be generated by excitation on the surface of the ground. These will propagate at different speeds. Thus multiple reflections can be expected. The dispersive nature of the Rayleigh wave will, furthermore, spread the input waveform in the time domain and thus introduce ambiguity into measurement of the time delay. It is therefore preferable to attempt to excite only one wave type.

The Rayleigh wave is unsuitable for attempting to detect targets at this depth as it is a surface wave, and as described by Equation 2.34, its amplitude will reduce rapidly with depth. This, coupled with the dispersive nature of the Rayleigh waves, mean that it is preferable that one of the two body waves be selected for the primary wave type of interest for the method.

Rayleigh waves have a lower input impedance than both the compressional and shear body waves [28]. Due to this it is likely that the Rayleigh waves will be of large amplitude relative to the body waves. For the very short time delays involved in this shallow seismic work this is potentially problematic; the small reflected body wave from the target may be obscured by the dominant Rayleigh wave component propagating along the surface of the ground. It is therefore preferable that the time interval between the arrival of the direct surface wave and the reflected body wave be large in order to ensure that the time delay between emission and reception of the reflected wave is not ambiguous or undefined.

Consider the scenario shown in Figure 3.1. A target object is buried at a depth h directly under the excitation source and a sensor placed in the same vertical plane at a variable horizontal distance s from the source. Using trivial geometry the time of flight for a wave propagating with speed c reflected from the target is given by

$$t(s) = \frac{h + \sqrt{h^2 + s^2}}{c} \tag{3.1}$$

Figure 3.2 shows Equation 3.1 plotted for a target object buried at 1.5 m for the two body waves and the direct Rayleigh wave propagating with typical wavespeeds. It can be seen that for the short horizontal distances to be used in this method the shear wave will be more easily differentiated from the Rayleigh wave. This is because the shear

and Rayleigh wavespeeds differ by only a small amount, whilst the compressional wave propagates much faster. Thus the large path difference between the direct and compressional waves for a small horizontal source-sensor displacement is compensated for by the high compressional wavespeed resulting in the waves arriving at the sensor close in time. It can be concluded that it is preferable to use shear waves when attempting to locate shallow buried objects close to the excitation source. For large source-sensor separations ($s \gg h$) the shear and Rayleigh wave time differences will become close and the compressional wave is preferable in target location.

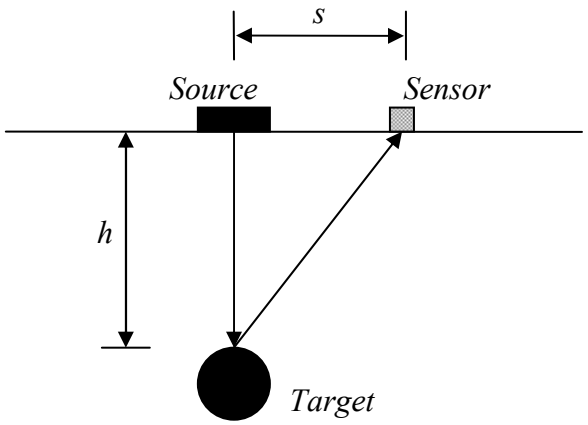

Figure 3.1 - Diagram showing target buried a distance *h* below excitation source with a sensor placed a variable horizontal distance *s* from it.

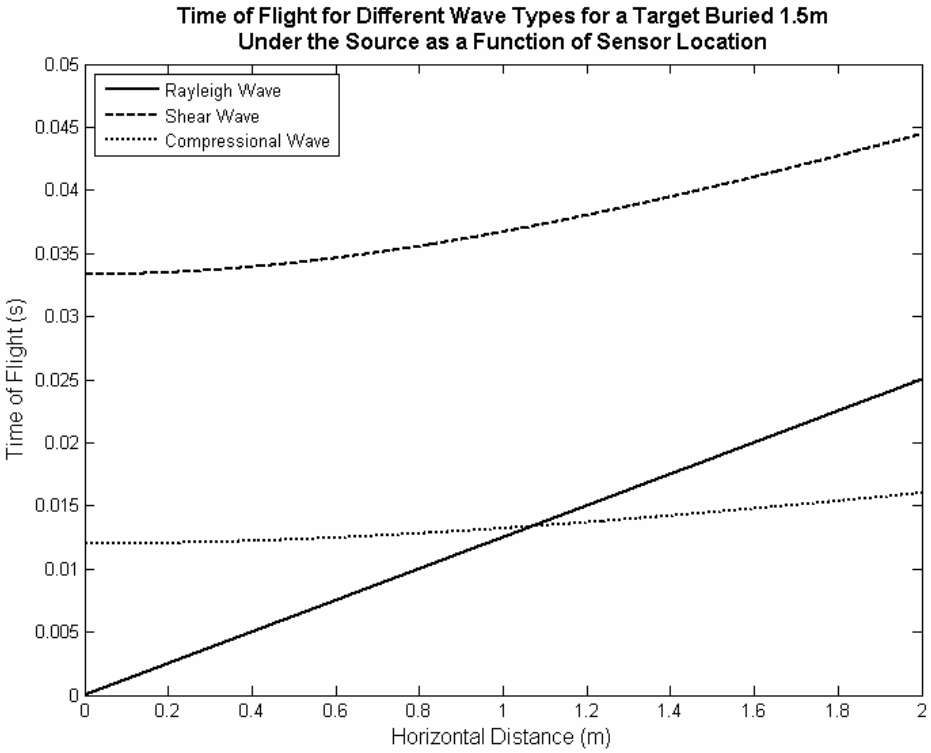

Figure 3.2 - Plot of the time of flight for various wave types for a 1.5 m target directly under the source. Assumed wavespeeds are $c_c = 250\ \text{ms}^{-1}, c_s = 90\ \text{ms}^{-1}, c_R = 80\ \text{ms}^{-1}$.

3.2 - Time Domain Stacking

The method of time domain stacking has been used in the location of shallow buried objects [42]. This method can be used to give a two-dimensional cross-sectional image through the ground (a B-scan image). The method of time domain stacking consists of a measurement procedure common to other methods followed by a specific post-processing algorithm to form the required image from the data.

The experimental procedure is as follows; an impulsive excitation source and an equally spaced line array of N geophones are placed along a measurement line. An outline of the experimental setup with relevant distances is shown in Figure 3.3. The experiment can be repeated with the source in different locations to ensure full illumination of non-point targets.

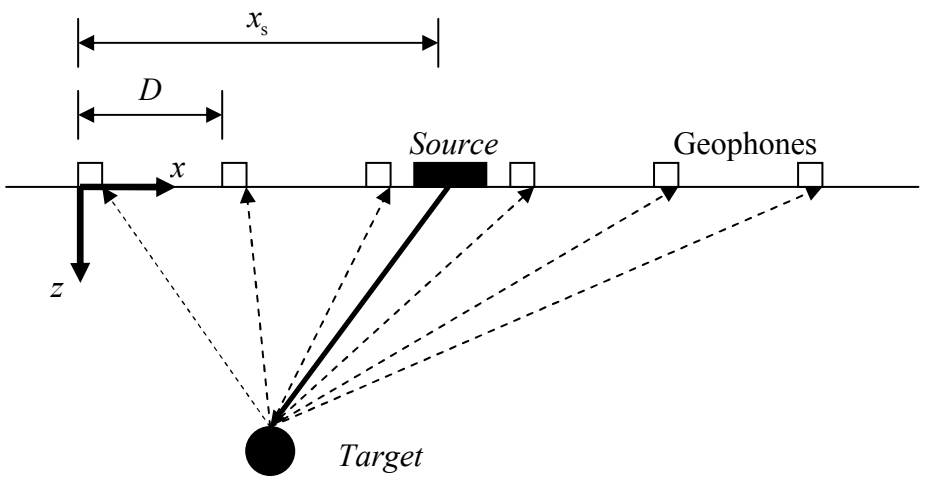

Figure 3.3 - Diagram of the experimental set-up. The origin of the coordinate system is on the ground surface at the location of the far-left geophone. The excitation source is represented as the solid rectangle and is shown in a central position, a distance x_s from the origin. The plain squares represent the geophones, separated by a distance D, and the solid sphere the target object. Point reflection is assumed.

The aim of the post-processing procedure is to form a cross-sectional image showing the spatial location of the areas of high seismic reflectivity from the numerous channels of time domain data. This is achieved by geometric considerations. The time of flight between the emission and reception of an input signal at the i^{th} geophone, located at a distance $x_{g,i}$, is given for a point reflector at an arbitrary location (x,z) by

$$t_i = \frac{1}{c}\left\{\sqrt{(x - x_s)^2 + z} + \sqrt{(x - x_{g,i})^2 + z}\right\}, \tag{3.2}$$

$$\text{where } x_{g,i} = D \times (i - 1), \qquad \text{for } i = 1...N.$$

The wavespeed is required to go from the time domain in which measurements were taken to the spatial domain required for imaging. It must therefore be measured in-situ as accurately as possible (see Section 5 for details on wavespeed measurement). For

the case of shear wave reflections $c = c_s$. All other quantities in Equation 3.2 are known from the experimental setup.

The image is formed by creating a matrix of points over the required cross-sectional area and considering each point individually. At each location the values of x and z are substituted into Equation 3.2 and a value for the time delay to each geophone obtained. The value of the time domain signal for each channel is taken at this time delay and added together. If this is the location of the target then every geophone should have a large signal at the locations in the time domain signals associated with the calculated time delays. If this is not the correct location then there will be contributions from only some, or none, of the geophone channels. Thus the correct location of the target should be represented by a maximum in the image.

3.3 - Improvements to the Post-Processing

In order to improve the quality of the image several post-processing additions to the method have been employed [40, 41].

3.3.1 - Enveloping Time Domain Signals

In reality a hammer blow or other such impulsive excitation will not produce a perfect impulse. The stiffness of the ground inevitably results in residual oscillations of the system. A typical geophone response to an impulsive excitation is shown in Figure 3.4. There are significant variations between positive and negative values at very short time delays from the main impulse. This causes cancellation of the reflected signal under stacking, thus reducing the target image.

To overcome this problem an envelope function has been fitted to the time domain signal and the envelope, rather than the time domain signal directly, has been stacked. No details have been provided by previous users of the method regarding the technique used to find the envelope function.

3.3.2 - Application of High Pass Filter

If the wavelength of the signal is much longer than the dimensions of the target object waves will propagate unimpeded and there will be little reflection. At wavelengths of approximately the same size as the target complex diffraction can be expected, causing poor reflection of the signal. Only at wavelengths smaller than the target will substantial reflection from the signal occur. As large wavelength, low frequencies components suffer from less attenuation than higher frequencies the low frequency non-reflected components can be expected to dominate the time domain data. As only the reflected components of the signals are of interest the signal to noise ratio can be enhanced by the removal of the low frequency data.

This can be achieved by passing the measured data through a high pass filter. The cut-off frequency of the filter will depend on the dimensions of the target under investigation.

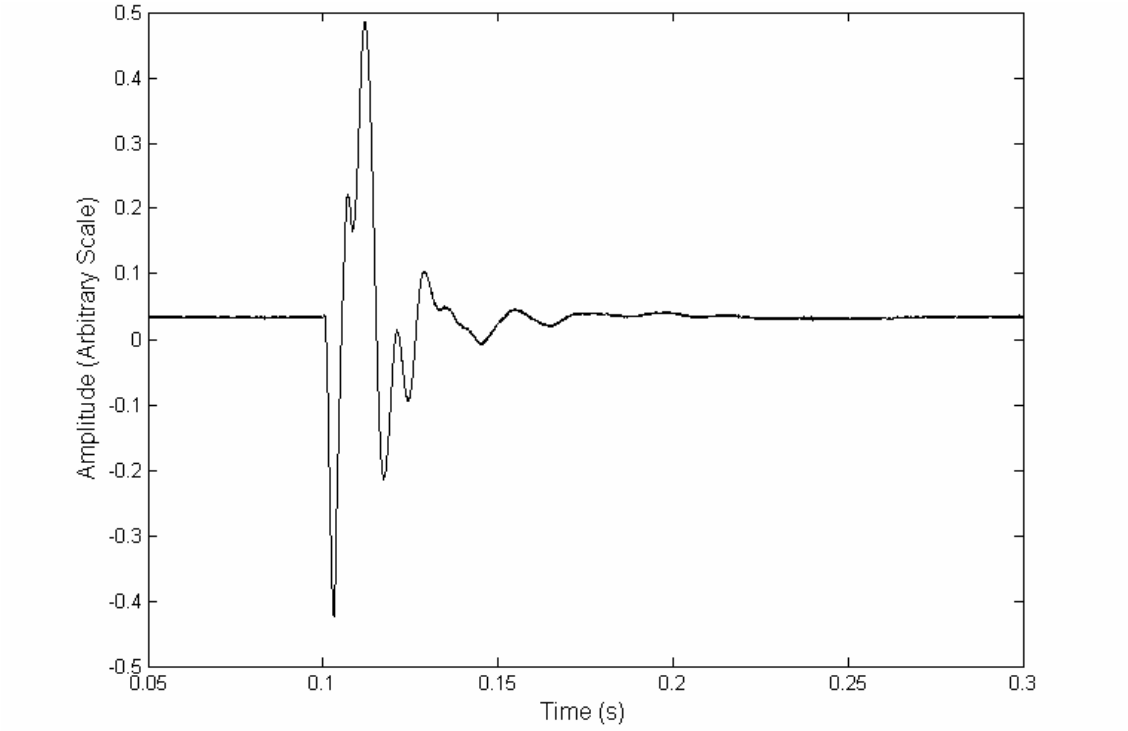

Figure 3.4 - Typical measured time domain response of geophone 0.25 m from an impulsive excitation with platform. For details on the experimental setup used in measurements see Section 5.

3.3.3 - Sensitivity Time Control

In order to counter attenuation previous users of the method have implemented the sensitivity time control (STC). This applies a weighting function to the time domain data that varies with the propagation distance. The weighting function is set to initially increase the value of the signal in order to counter attenuation. The rate of increase must be set empirically or approximate measurements taken in-situ to determine an average attenuation rate.

For a large propagation distance the reflected signal is likely to have become heavily attenuated and lie below the noise floor. As such, boosting the relative level of the signal will not improve the image, as only noise will be given the increasing prominence. The STC is therefore set such that after a given propagation distance the weighting function begins to fall off to reduce the effect of the noise contaminated signal. Again the propagation distance after which the weighting function is reduced and the rate of fall off past this distance must be determined empirically or approximated from in-situ measurements.

This method, whilst previously implemented with some success, does fail to take into account certain important factors. There will be substantial variation of the attenuation with frequency, with the attenuation rising for high frequencies. The STC fails to take this into account and offers only a single value of attenuation compensation for all frequencies.

In practice the values defining the cut-off and gradients of the STC weighting function will also have to be decided upon somewhat arbitrarily. Variation between sites will prevent a general weighting function. Previous implementation of the STC

has been undertaken manually after measurement and is not suitable for automation required for efficient use of the method.

3.4 - Discussion of the Algorithm

The image produced by the time domain stacking procedure is now considered. For this purpose the function used to calculate the time delay between emission and reception can be examined. Assume a single sensor located a distance x_g recording a time data series $y(t)$. Assume further that a perfect impulse is produced and that non-dispersive propagation and perfect reflection cause no distortion of the waveform between emission and reception. Thus

$$y(t) = \begin{cases} 1 & t = \tau \\ 0 & t \neq \tau \end{cases} \tag{3.3}$$

where τ is the time delay and the magnitude of the impulse is arbitrary and has been set to unity for convenience. Rearrangement of Equation 3.2 gives the relationship between the coordinates in terms of the time delay between emission and reception for a given geophone;

$$z(x) = a_1 x^2 + a_2 x + a_3, \tag{3.4}$$

where the coefficients of the polynomial terms are;

$$a_1 = \left(\frac{x_s - x_g}{ct} \right)^2 - 1, \qquad a_2 = \frac{(x_s - x_g)\left[(ct)^2 + (x_s^2 - x_g^2) \right]}{(ct)^2} + 2x_s,$$

$$a_3 = \left[\frac{(ct)^2 + (x_s^2 - x_g^2)}{2ct} \right] - x_s^2 .$$

For the impulsive signal there will only be non-zero contributions to the image when $t = \tau$. It can be seen by substitution of $x = x_s = x_g$ that for the trivial case of a target directly below a coincident source and geophone the depth of the target is simply half the total distance travelled, as is to be expected. A single geophone with a perfectly impulsive signal will, by Equation 3.4, produce a parabolic image such as that in Figure 3.5. This shows that a single geophone can provide no directional information; only the distance travelled can be inferred. As the time delay τ will be different for each geophone location the stacking procedure sums multiple parabolas onto the image. The target lies where all these parabolas are consistent i.e. at their intersection. In theory the use of only two geophones would be enough to locate a buried reflector. In practice the use of more geophones will give a greater on/ off target contrast and provide better spatial resolution.

The wavespeed is unlikely to be known to a high degree of precision. As the wavespeed scales the measured time delays the effect of an under/over estimated

wavespeed will be to cause contraction/expansion of the parabolas in the image respectively. For the ideal impulses this will result in no point in the image in which the parabolas coincide. Realistic impulsive excitation, however, will not provide an infinitely sharp peak; there will be an extended time response. The parabolas produced in the image will thus posses a width that will depend on the duration of the impulse excitation. Small deviations in the wavespeed will therefore lower the on/ off target contrast, rather than completely obscure the target.

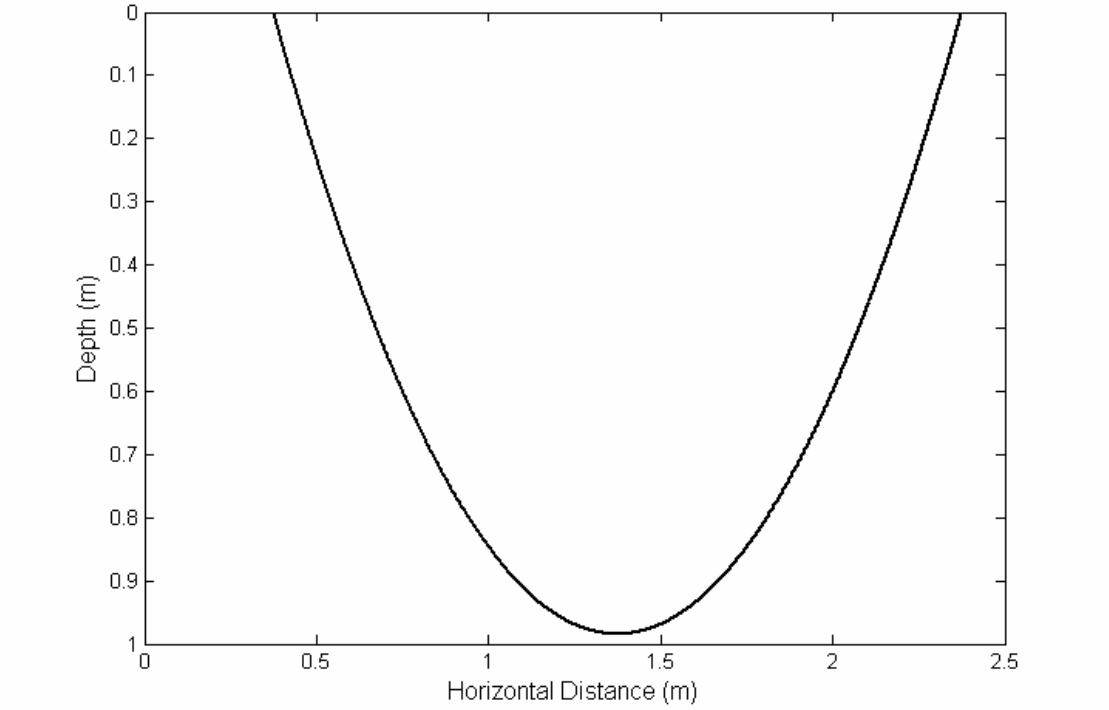

Figure 3.5 - Image produced by Equation 3.4 considering one geophone and a perfectly impulsive signal. The source was located at 1.25 m from the origin and the geophone 1.5 m, with a target depth of 1 m. The horizontal distance and depth correspond to the *x* and *z* coordinates respectively.

As outlined in Section 3.1 only the shear wave is desired for considering the reflections from shallow buried objects. However compressional waves will still be produced and may be of notable magnitude. If there are two peaks in the measured time data then each geophone will produce two parabolas on the image. Provided the shear wave speed is used in the implementation of the method then the compressional parabolas will be contracted towards the surface (as they always travel faster than the shear wave) and will therefore not coincide at a false target location. For many geophone signals summed the effect of the compressional wave reflections on the image will be to increase the magnitude of the image at depths shallower than the target and thus lower the on/off target contrast. A false image will not be created.

3.5 - Limitations of the method

The main limitation on the method discussed in this section is its reliance on an impulsive waveform for excitation. Impulses suffer from several important limitations. There is poor control over the frequency content of the signals. Whilst some variation can be obtained by varying the material of the hammer tip this can offer only general variation in the frequency content. Furthermore for impulsive signals all the energy of the signal is inputted into the system during a very short period of time. This constrains the energy input to the system before the amplitude of motion becomes large enough for non-linearities to arise.

Repeatability of the impact may also be difficult. When stacking multiple recordings to form an image it is important that the excitation source remains unchanged throughout the different runs. Whilst good repeatability may be obtainable with the use of a mechanical impact rig this may prove impractical for field experiments.

Section 4 - Extended Signals & Correlation Domain Stacking

4.1 - Advantages and Selection of Time Extended Signal

To overcome some of the limitations of the method outlined in Section 3.5 an extended rather than impulsive excitation can be used. Time extended signals produced by a transducer have the advantage that the waveforms can be controlled arbitrarily and possess frequency components limited only by the quality of the transducer and sample and bit rate used in signal generation. By extending the signal in time more energy can be put into the system without the amplitude of the motion exceeding the linearity range.

The extended signal chosen for use is a chirp. In order to cover the frequency range of interest evenly a linear chirp was chosen. For a sweep from frequency f_1 to f_2 in a period of time T the frequency is required to vary with respect to time as

$$f(t) = f_1 + \frac{f_2 - f_1}{T} t . \tag{4.1}$$

The instantaneous frequency is defined as the rate of change of the phase angle φ;

$$f(t) = \frac{\partial \varphi(t)}{\partial t} \qquad \Rightarrow \varphi(t) = \int f(t)\, dt . \tag{4.2}$$

The variation of phase with respect to time for a linear frequency sweep is given by the substitution of Equation 4.1 into Equation 4.2. This gives the desired phase as a function of time as

$$\varphi(t) = t\left(f_1 + \frac{f_2 - f_1}{2T} t \right) + \text{constant} . \tag{4.3}$$

The sensors to be used for measurements are geophones, which measure velocity. If an acceleration chirp were to be used as an excitation waveform then the geophones would measure, even in ideal propagation conditions, a response that reduces with frequency. This would reduce the effective bandwidth of the signal, which has the undesirable implications described in Section 4.2.2. It is therefore sensible to input a velocity chirp into the system. The required velocity of the excitation source, $v(t)$, is thus given by

$$v(t) = V_0 \sin\left[2\pi t \left(f_1 + \frac{f_2 - f_1}{2T} t \right) \right], \tag{4.4}$$

where V_0 is the amplitude of the input. The constant term of Equation 4.3 can be set arbitrarily as the initial phase of the chirp will not alter the frequency content of the waveform. The shaker to be used is however electromagnetic in nature and as such has an acceleration output approximately proportional to the voltage input in the frequency range of operation.

The required voltage to be provided to the shaker to generate a velocity chirp of amplitude A_0 is therefore

$$a(t) = \frac{dv(t)}{dt} = A_0 \cos\left[2\pi t\left(f_1 + \frac{f_2 - f_1}{2T}t\right)\right], \tag{4.5}$$

where $A_0 = V_0\left[2\pi\left(f_1 + \left(f_2 - f_1\right)tT^{-1}\right)\right]$.

Although chirps will be used as the extended signal in the work discussed here, other extended signal types are possible. Stepped sinusoids are used in many measurements. For a stepped sine input a single frequency is outputted for a relatively long period of time (many cycles of the waveform) before the frequency is discontinuous changed to another frequency. The frequency intervals are usually chosen in octave or third octave bands to equally cover a given frequency spectrum. A continuous sinusoid will not be an appropriate for the time-domain reflection measurements as it is a periodic input. It is shown in Section 4.2 that periodic inputs fail to meet the requirements for application to the proposed method.

The use of random signals as inputs to the system has also been considered. These meet the criteria of covering a wide frequency range in a non-periodic manner, and could therefore be used satisfactorily in the proposed method. However the correspondence between the time and frequency domains provided by the chirp gives the latter precedence in application of the method.

The use of time extended signals prohibits the use of the time domain stacking method described in Chapter 3. This is because the time domain stacking method relies on the measured signal having significant value only at a time delay equal to the difference between the emission of the waveform at the source and its reception at the sensor. Whilst some deviation from a perfect impulse is permissible (see Section 3.3.1) this deviation must be small compared to the time delays in the system and preferably reduce quickly in time. If this is not the case then values of the coordinates of the image space which do not correspond to the location of a reflector could have large values, thus obscuring the target. An extended signal such as a chirp will violate this condition. A different approach to the stacking must therefore be undertaken with the aim of producing a sharp peak at a time equal to that of the delay between emission and reception. To this end cross-correlation functions are used. These are described in the following section.

4.2 - Basic Cross-Correlations (BCC) Functions

Cross-correlation functions are widely used in signal processing applications for assessing the similarity of two signals. The basic properties of the functions shall be described first, with specific attention then given to the consequences of cross-correlating low bandwidth signals.

4.2.1 - Definitions and Basic Properties

The cross-correlation as a function of the relative delay between two zero-mean signals $x(t)$ and $y(t)$ is defined as

$$R_{xy}(\tau) = \lim_{L\to\infty} \frac{1}{L} \int_0^L x(t)\, y(t+\tau)\, dt\,, \tag{4.6}$$

where τ is a variable in time measuring the relative time lag between signals and L is the length of the signal. To obtain an exact cross-correlation function requires an infinite period of measurement, which is obviously not physically realisable. As such the limit shall be omitted with the understanding that the resultant cross-correlation function will be only an estimate of the exact cross-correlation function.

The cross-correlation function can be physically interpreted as follows. The signal $y(t)$ is shifted over the signal $x(t)$, with the shift given by the lag variable τ. At each value of τ the cross-correlation is the integral of the product of the two signals. If the signals are dissimilar at a given value of τ then their product will be both positive and negative in approximately equal amounts and thus the integral of the product will be small. If the signals are similar at a particular time shift then their product will mainly positive and the integral of the product will be large. If the signal $y(t)$ is a delayed replica of $x(t)$ then at a value of τ equal to this delay the cross-correlation will be maximal. Thus the value of cross-correlation gives a quantitative value of the similarity of two signals.

A special case of the cross-correlation function is the auto-correlation function. This is where a signal is correlated with itself. Equation 4.6 becomes

$$R_{xx}(\tau) = \int_0^L x(t)\, x(t+\tau)\, dt\,. \tag{4.7}$$

Note that as the two signals being correlated are identical there must be a maximum value at time delay $\tau = 0$, as the integral will be over an entirely positive product. Furthermore as they are identical the direction of the shift is irrelevant. The autocorrelation is therefore symmetric about a maximum in the null shift.

If the reflection of a waveform occurs in a medium in which there is no distortion of the waveform and therefore results in only a time delay τ_0 and an amplitude scale factor A between the measured signal $y(t)$ and the input signal $x(t)$ then the two are related by

$$y(t) = Ax(t - \tau_0)\,. \tag{4.8}$$

Substituting Equation 4.8 into the definition of the cross-correlation given in Equation 4.6 gives the cross-correlation function for reflection in an ideal medium to be;

$$R_{xy}(\tau) = \int_0^L x(t)\, Ax\left(t + (\tau - \tau_0)\right) dt\,,$$

$$= AR_{xx}(\tau - \tau_0)\,. \tag{4.9}$$

As the auto-correlation function has maximum amplitude when its shift variable has a zero value Equation 4.9 shows that the cross-correlation function for a single reflection in an ideal medium will have maximum amplitude at a value of the time shift variable equal to the time delay between signals.

It should be noted that the auto-correlation of a periodic input (and therefore the cross-correlation of a periodic signal with a delayed version of itself) will not produce a single peak in the correlation domain. There will be a high degree of correlation at time intervals equal to the period of the signal. However there will still be a global maximum in the auto-correlation function at a lag of zero.

A related function is the cross-spectral density, which for time signals $x(t)$ and $y(t)$ is denoted by $S_{xy}(f)$ and defined by

$$S_{xy}(f) = X^*(f)Y(f)\,, \tag{4.10}$$

where the asterix denotes the complex conjugation, and $X(f)$ and $Y(f)$ are the Fourier transforms of $x(t)$ and $y(t)$ respectively. If the two signals are identical the result is known as the auto-spectral density and reduces to the magnitude squared of the signals' Fourier transform.

It can be shown via the generalised Wiener-Khinchin theorem [59] that the cross-spectral density and the cross-correlation function form a Fourier transform pair:

$$S_{xy}(f) = F^{-1}\left\{R_{xy}(\tau)\right\} = \int_{-\infty}^{\infty} R_{xy}(\tau) e^{j2\pi f\tau} d\tau\,, \tag{4.11}$$

where F^{-1} denotes the inverse Fourier transform. Conversely if the cross-spectral density has been measured then an estimate of the cross-correlation can be obtained from

$$R_{xy}(\tau) = F\left\{S_{xy}(f)\right\} = \int_{-\infty}^{\infty} S_{xy}(f) e^{-j2\pi f\tau} df\,, \tag{4.12}$$

where F denotes the Fourier transform.

4.2.2 - Bandwidth Limitations

The two requirements for a signal to be suitable for the stacking method are that there is a peak at the correct time delay and that this peak is narrow relative to the time delays of interest. The first of these constraints has been shown but the latter is equally important, else there will be poor resolution of reflected signals in the correlation domain.

The cross-correlation function of bandlimited signals is now examined. The derivation is given in Appendix B and the final result simply stated. The cross-correlation function of a signal which is spectrally flat over a bandwidth *b* with central frequency f_0 and amplitude *M* with a identical waveform delayed by time τ_0 and whose frequency amplitude is scaled by a factor *C* is given by

$$R_{xy}(\tau) = MbC\,\mathrm{sinc}\left[\pi b(\tau - \tau_0)\right]\cos\left[2\pi f_0(\tau - \tau_0)\right]. \tag{4.13}$$

This is a cosine function whose frequency varies with the central frequency of the input waveform and which is enveloped by a sinc function whose frequency varies with the bandwidth of the input waveform. In order to examine the width of the cross-correlation function the location of the first zero of the envelope sinc function is considered. This occurs when the argument of the sinc function is equal to π. This imposes the condition that;

$$\pi b(\tau - \tau_0) = \pi$$

$$\Rightarrow \tau_{1^{st}\mathrm{zero}} = \tau_0 + \frac{1}{b}. \tag{4.14}$$

Equation 4.14 shows that as the bandwidth tends towards infinity the first zero tends towards the centre of the sinc function, which will occur at τ_0. The cross-correlation function is therefore tending towards an infinitely sharp peak. Conversely when the bandwidth becomes small the width of the central peak in the cross-correlation function becomes large. Figure 4.1 shows the cross-correlation function for two signals of both high and low bandwidths. The variation in central peak width is evident.

This is significant for two reasons; firstly wide cross-correlation peaks will result in poor spatial resolution and under the stacking method produce poor images. Secondly if there is more than one correlated version of the input in the measured waveform multiple peaks in the cross-correlation function will result. For low bandwidth signals resolution in the correlation domain would therefore be poor, resulting in ambiguity of the time delay intervals and allowing the possibility of small correlation peaks being obscured completely.

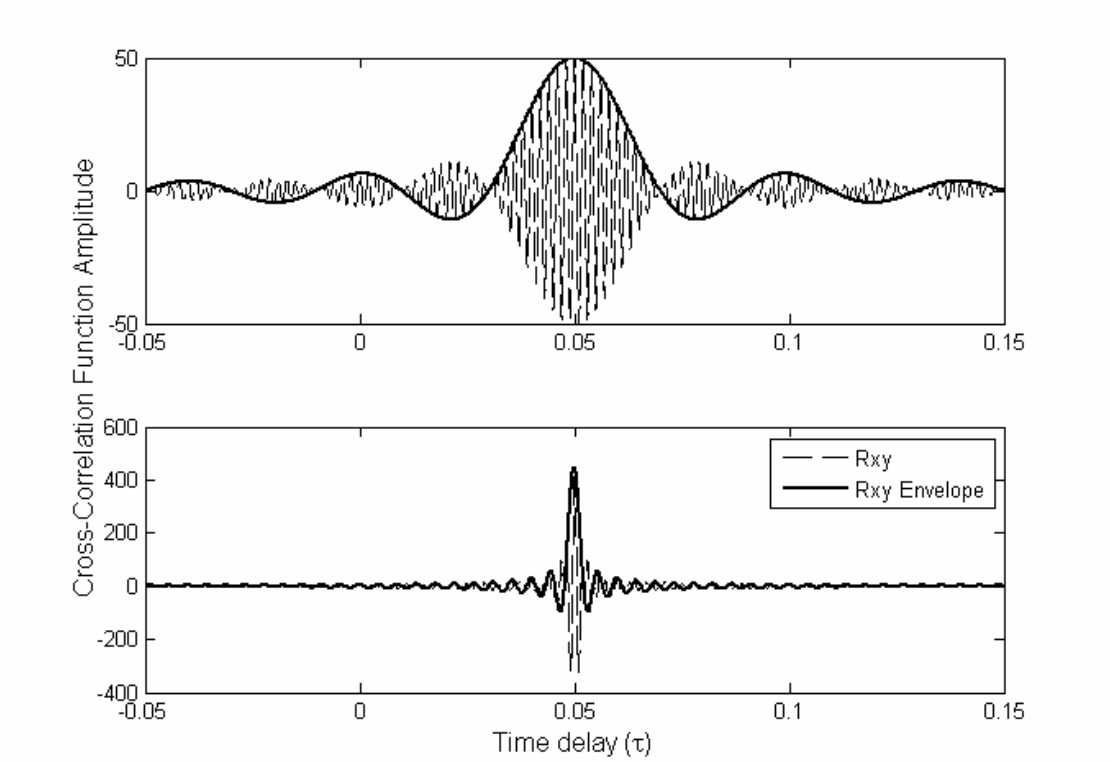

Figure 4.1 - Plot of the theoretical cross-correlation function between two identical bandlimited signals with a relative delay of 0.05 seconds. The result was obtained by implementation of Equation 4.13. The envelope of the cross-correlation function is shown by the heavy line. The bandwidth of the upper panel signals is 50 Hz and the bandwidth of the lower panel signals is 450 Hz. Both have a centre frequency of 500 Hz. Note the differing scales of the y-axis.

A further benefit of increased bandwidth is that the cross-correlation is proportional to the bandwidth, as shown in Equation 4.13. Increasing the bandwidth therefore increases the maximum amplitude of the cross-correlation function. It can be concluded that in order to achieve optimum results it is necessary to attempt to maximise the bandwidth of any signals to be correlated.

The relationship between the correlation peak width and the bandwidth of signals can be explained by considering the cross-spectral density approach to cross-correlation function estimation. Combination of Equations 4.10 and 4.12 gives the relationship between the cross-correlation function and the Fourier transform of the two signals to be;

$$R_{xy}(\tau) = F^{-1}\left[X^*(f)Y(f)\right]. \tag{4.15}$$

If the signals $x(t)$ and $y(t)$ are bandlimited then the product of their Fourier transforms will give a result that is of limited extent in the frequency domain. Upon Fourier transforming to obtain the cross-correlation function this band limiting is effectively acting as a windowing function in the frequency domain. Thus the cross-correlation function will be multiplied by the Fourier transform of this windowing function. The uncertainty principle states that the product of the bandwidth of a signal and its spread in time must exceed a fixed limit [59]. Thus the narrower a function the wider its Fourier (or inverse Fourier) transform will be. This means that the narrower

the bandwidth limitation on the original signal the narrower the effective window when Fourier transforming the signal will be, resulting in a greater spread in the cross-correlation function. In the ideal band limiting case where the gradient of the cut-off in the frequency domain is infinite, the signal is being windowed by a boxcar function. As the Fourier transform of a boxcar function is sinc function the expression obtained for the cross-correlation function in Equation 4.13 is multiplied by a sinc function.

Section 4.3 - Generalised Cross-Correlation Functions

It has been shown in the previous section that limited bandwidth leads to poor resolution in the correlation domain. The ground under vibration exhibits strong attenuation of propagating waves that increases with frequency and as such the frequency content of the received waveforms is unavoidably constrained. This will lead to a widening in the cross-correlation peaks with the associated undesirable effects.

In order to narrow cross-correlation peaks several variations of the cross-correlation function have been proposed, referred to collectively as generalised cross-correlation functions (GCC). These can be defined in general terms by adding a weighting function to the integrand of Equation 4.12 [60];

$$R_{xy}(\tau) = F\left\{\Psi(f) S_{xy}(f)\right\} = \int_{-\infty}^{\infty} \Psi(f) S_{xy}(f) e^{j2\pi f\tau} df, \tag{4.16}$$

where the weighting function $\Psi(f)$ depends on the type of GCC in use. A specific example is the phase transform (PHAT) which is defined by the weighting function;

$$\Psi_{\text{PHAT}}(f) = \frac{1}{\left|S_{xy}(f)\right|}. \tag{4.17}$$

This, therefore, divides the cross-spectral density by its magnitude, thus destroying all magnitude information whilst preserving the phase information. The effective bandwidth of the signal is therefore maximised, reducing the width of the central peak of the cross-correlation function. Physically the destruction of the magnitude data can be justified as only relative delays, and therefore only phase, not magnitude information, is relevant to the problem. Moreover the phase information is more robust to noise contamination, as in order to unwrap the phase information the variance of the noise must be above the 2π jump that occurs when the phase of the waveform enters an additional cycle. It should be noted that in regions where the signal to noise ratio is poor the decrease in the width of the correlation peak may come at the expense of a reduction in its amplitude and the accuracy of its location, as the PHAT will serve only to boost noise.

In order to reduce the problem of the PHAT boosting regions of low signal to noise ratio the smoothed coherence transform (SCOT) can be used. This is defined by;

$$\Psi_{\mathrm{SCOT}}(f) = \frac{\gamma_{xy}(f)}{\left|S_{xy}(f)\right|}, \tag{4.18}$$

where $\gamma_{xy}(f)$ denotes the coherence function and is given by;

$$\gamma_{xy}(f) = \left[\frac{\left|S_{xy}(f)\right|^2}{S_{xx}(f)S_{yy}(f)}\right]^{1/2}. \tag{4.19}$$

The SCOT thus fixes the magnitude of all frequency content to unity and then multiplies by the coherence function of the two signals. Frequency regions of low coherence are thereby reduced. As the coherence is a measure of the similarity of two signals this has the effect of increasing the effective bandwidth of the signal with preference to the regions of high signal to noise ratio.

The validity of the GCC techniques is demonstrated by a simple simulation resulting in the cross-correlation functions given in Figure 4.3. For this two exponentially decaying chirps with equal decay rate and magnitude were cross-correlated both with the BCC and the PHAT implementation of the GCC. The time histories of the two chirps are shown in Figure 4.2 and their cross-correlation in Figure 4.3. It can be seen that when using the BCC (Figure 4.3a) the bandwidth of the resulting function is large, as the attenuation reduces the effective bandwidth prior to application of the cross-correlation. Application of the PHAT (Figure 4.3b) has the desirable effect of reducing the bandwidth to that obtained if the chirps are not attenuated (Figure 4.3c).

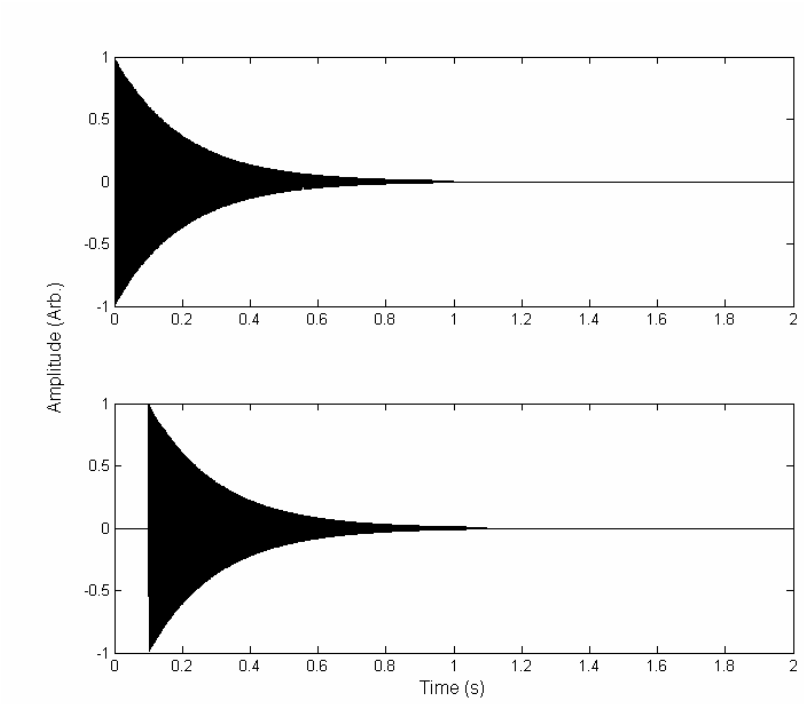

Figure 4.2 - Plot of the time histories of the two decaying chirps used to illustrate the effects of the phase transform. Both chirps contained linear frequency variation between 475 and 525 Hz and an exponential decay constant was five. The offset was 0.1 seconds.

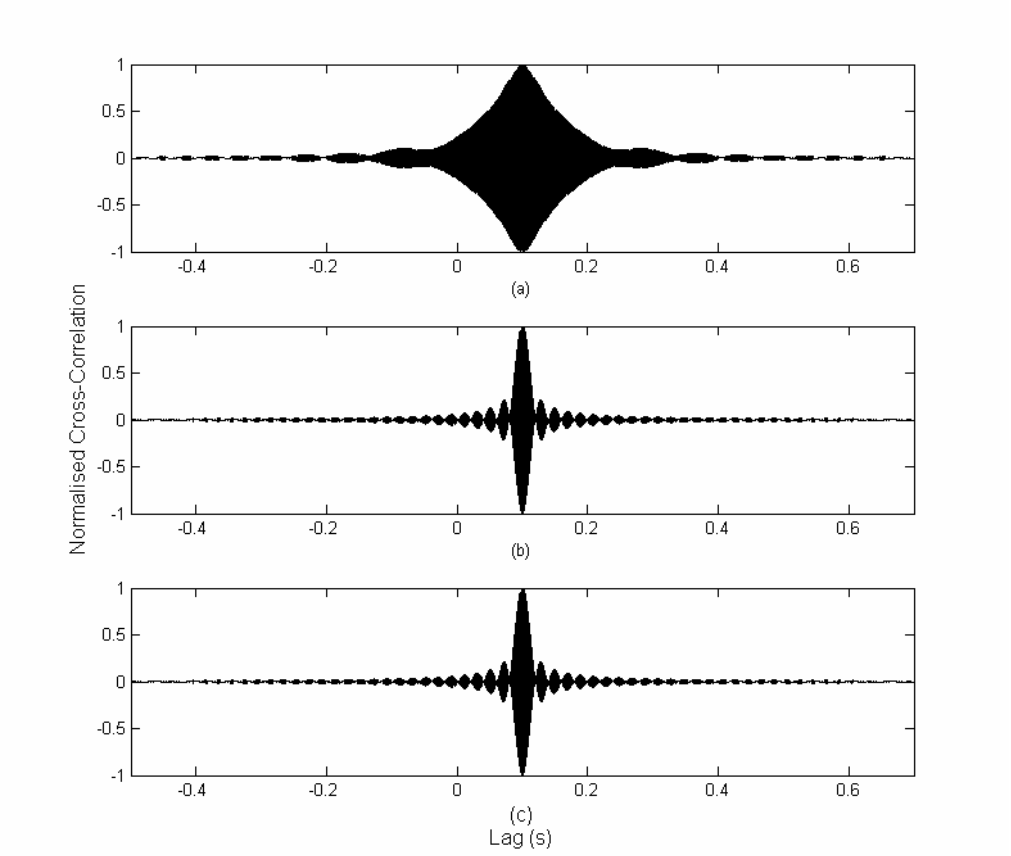

Figure 4.3 - Plot of the cross-correlation between two exponentially decaying chirps both with (a) BCC (b) PHAT GCC (c) BCC on chirps without decay for comparison.

4.4 - Practical Implementation of Cross-Correlation Functions

In order to enable the use of time extended signals the stacking method described in Section 3 can be modified by stacking cross-correlation functions rather than the time domain signals directly. For this to produce the correct image the peak of the cross-correlation function must be at a time delay corresponding to the time between the emission of the waveforms from the shaker and the reception of the waveform at the geophones. The measured geophone signal must therefore be cross-correlated with a reference signal synchronous with the waveform emission. This adds an extra channel of measurement to the time domain stacking method.

Several possible reference signals exist. The waveform inputted to the shaker could be recorded and used. This technique is used in radar [54], partly because of the difficulty in measuring the waveform after emission and partly so that matched filters can be used to give an effective hardware implementation of the method. Use of the input waveform has the advantage that the bandwidth will be optimally wide and therefore minimise the width of the cross-correlation peak. It will, however, not take into account the magnitude and phase changes caused by both the inadequacies of the transducer and the interaction of the shaker, platform and ground. The platform is likely to have internal resonances, and the local properties of the ground will act as a stiffness producing a resonant system. The actual waveform inputted into the ground may therefore substantially vary from the electrically inputted waveform.

The output of an accelerometer built into the shaker could be used. This would have the advantage of taking into account of the interaction of the shaker, platform and ground. This has the disadvantage that only the acceleration, not the velocity, can be measured. As such numerical integration of the signal would have to be undertaken before cross-correlation techniques could be performed.

A final possibility is the use of a reference geophone. This would be located as close to the platform as possible to measure the signal before significant attenuation could occur. The shaker, platform and ground interaction would be taken into account and as a geophone would be used the output would be a measurement of velocity. This would have the disadvantage of bringing the directionality of the shaker into the measurement. Furthermore the wave propagation over the surface of the ground may be different to that of the body waves propagating to and from the target. Cross-correlation with this reference may therefore be more likely to pick out surface waves in the received geophone signals than reflected body waves as desired.

4.5 - Wavespeed Measurement and the Cross-Correlation Method

In order to be able to implement the stacking method it is necessary to have an estimate of the wave speed of the relevant wave in the medium. A poor wavespeed estimate will reduce the contrast of the target in the image and possibly result in the failure of the correlation peaks associated with the target reflection from each geophone to intersect at a point. A variety of wavespeed measurement techniques exist in the literature [61], however many of these concern themselves with more complex techniques such as velocity depth profiling. In order to measure the body wave speed one of two methods can be taken; either the body wave can be measured directly or indirectly via the surface wavespeed. In both cases the aim is to measure

the time of propagation of a known waveform between a source and sensor of known separation, thus enabling calculation of the wavespeed.

For the case of direct measurement either a source or sensor must be located under the surface of the ground. Previous users of the stacking method have performed wavespeed measurements by striking a pole pushed into the ground, thus producing a source under the surface [42]. This option however prohibits selection of a specific body wave and is likely to lead to production of both compressional and shear waves, possibly impeding accurate measurement. Alternatively a sensor could be inserted into the ground at a known distance from the source and the surface excited using the shaker and platform. This would have the advantage of being able to preferentially excite certain wave types. Forcing a transducer under hard soils may however prove difficult.

The former of these cases, where the source is a simple impulse under the surface of the ground is not recommended as in order to use correlation functions the input waveform must also be measured requiring a transducer to be buried with the source. If this is done the source may as well be located on the surface and the transducer under the ground. For this set-up the excitation waveform, measured in one of the ways outlined in Section 4.4, could be cross-correlated with the buried transducer output in order to gain a value for the time interval between emission and reception.

Indirect body wavespeed measurement can be achieved by measuring the speed of the surface wave and using numerical solutions to Equation 2.31 to obtain estimates for the body wave speeds. The wavespeed can thus be inferred in-situ without penetration of the surface and by cross-correlating two geophone signals of known separation arranged inline with the source. An identical experimental set-up identical to that used in the stacking procedure can be used for this measurement.

In order to obtain the wavespeed of the body waves the Poisson's ratio of the medium must be known. It is unlikely that this can be measured in situ, and would therefore have to be assumed depending on the soil type. This is more problematic for obtaining the compressional than the shear wavespeeds, as the ratio of the Rayleigh to shear wave velocities has only weak Poisson's ratio dependence, varying between 0.88 and 0.96 over the possible range of the Poisson's ratio [62]. The ratio of the Rayleigh to compressional velocities however has much stronger dependence on the Poisson's ratio, varying between 0 and 0.6. This method is therefore more suited to the measurement of shear waves.

Section 5 - Experimental Work

5.1 - Experimental Site

Experimental work was performed for two days in May of 2008 at a Ministry of Defence site in Essex. The site was located on a large open training facility and consisted of a network of interconnecting pipes used for confined space training. These were made of concrete and were approximately one metre in diameter and buried approximately one metre deep. The tunnels had access points at each end and could be entered.

The ground suffered from small undulations, of the order of ten centimetres, probably due to the settling of the ground after the pipe burial. There were also notable cracks in the ground's surface. The area was covered with short grass. As the pipes had not been buried for the purposes of shallow seismic surveying it is likely that little care was taken in removing debris from the soil used to fill the pipes in. In several places concrete debris was visible at the surface.

Soil samples were not taken due to time constraints. It was however observed when digging shallow holes that the upper layer of ground was clay and seemed reasonably homogeneous. The underlying substructure was unknown.

5.2 - Experimental Equipment

The experimental equipment setup is shown in Figure 5.1. The input chirp signal is produced by a Hameg HM8130 signal generator and outputted to the power amplifier. The power amplifier is designed specifically for the shaker with both produced by Wilcoxen Research. The shaker is an F4 inertial electromagnetic transducer and contains a built in force gauge and accelerometer. These are powered by the amplifier and their outputs require no additional amplification.

The geophones used are Input/Output SM-9's with a sensitivity of 28.8 V/ms^{-1}. These are electromagnetic in nature and consist of a coil surrounding a magnet. Relative motion between the coil and magnet induces a voltage in the coil which is proportional to the velocity [2] along the given axis. Both vertical and horizontal geophones were available. These, along with the shaker accelerometer and force signals are sent to the data acquisition unit. For time domain measurements an eight channel Prosig P8000 data acquisition unit was used. A four input channel DataPhysics Signalcalc ACE data acquisition unit was also available for use and was mainly used for transfer function measurements. All power was provided by a petrol generator located approximately 50 metres from the experiment.

The use of a signal generator was not ideal as only standard waveforms were available for use. However it was found during field testing that the equipment configuration required to enable the use of custom signals resulted in poor grounding and high levels of electrical noise. This prevented measurement of small signals. Furthermore as the noise was electrical in nature it was identical on all channels and correlated perfectly. This had the ability to obscure any peaks in cross-correlation functions and thus destroy the information necessary to form an image.

It has been shown [28] that a vertical excitation on the ground's surface will cause most (67%) of the input energy to go into Rayleigh waves, with 26% for shear waves and perhaps un-intuitively only 7% of the input energy goes into compressional waves. In order to ensure that the energy going to the shear wave is maximal the ground can be excited via a platform rather than simply striking the surface of the ground. Such a platform consists of a horizontal base plate with prongs protruding from the bottom. The prongs of the platform are pushed into the ground so that the base sits flush with the grounds' surface. The platform can then be stuck from the side of the plate to cause an impulsive shear excitation.

A photograph of the platform used is shown in Figure 5.2. The shaker can be bolted to the either the base plate or a plate perpendicular to it. When the shaker is bolted to the base plate excitation will occur in a direction perpendicular to the surface of the ground. This position shall be referred to as the compressional position of the platform, as the motion is consistent with the generation of compressional waves (although as stated above little energy will actually go into the generation of compressional waves). When the shaker is bolted to a plate perpendicular to the base plate excitation will occur in a direction parallel to the surface of the ground. This position is referred to as the shear position of the platform, as the motion is consistent with the generation of shear waves.

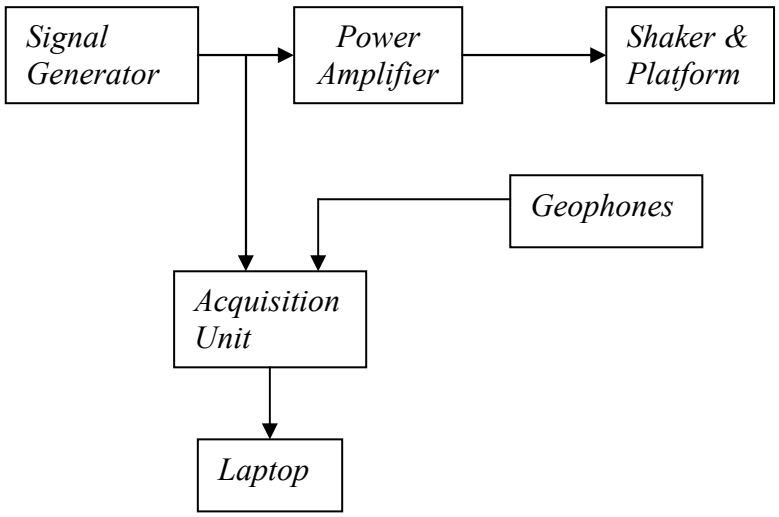

Figure 5.1 - Block diagram of the experimental setup used.

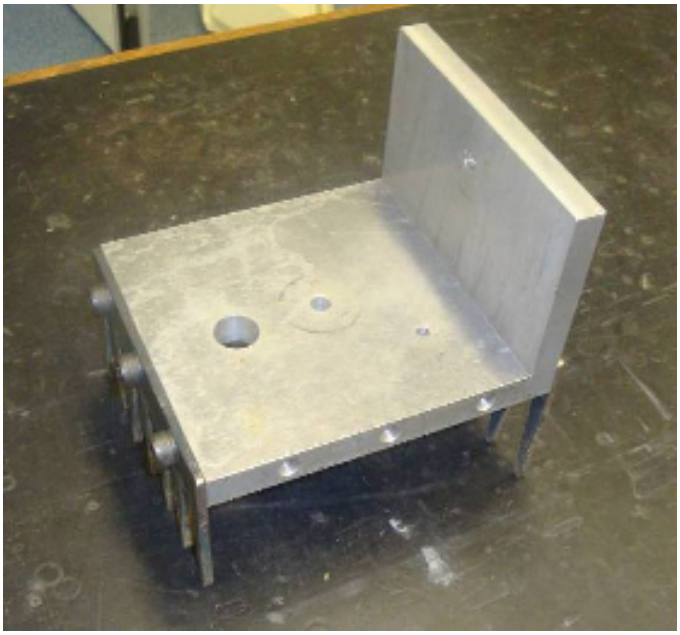

Figure 5.2 - Photograph of the shaker platform used throughout experimentation.

5.3 - Shaker and Platform Directivity

The shaker and platform will interact in a complex manner with the ground during excitation. Preliminary experiments were therefore conducted at the site in order to asses the ability of the shaker/platform system to transmit the desired signal into the ground. As the platform is likely to exhibit some directivity, multiple geophones must be used. The experimental setup is shown in Figure 5.3. The shaker has four geophones placed as close as possible around it in order to measure the ground motion both perpendicular and parallel to the excitation motion on two adjacent sides of the platform.

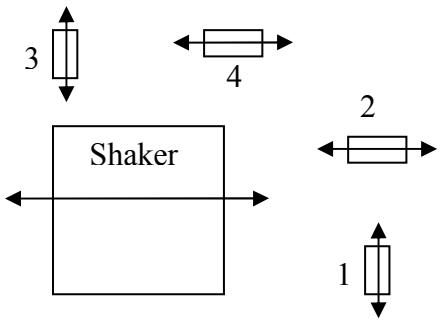

Figure 5.3 - Experimental setup used to asses the directivity and coupling of the platform to the ground. All geophones had their sensitive direction oriented parallel to the horizontal plane. Arrows indicate the axis of shaker excitation and of geophone sensitivity.

Measurements were made with a linear chirp with frequency content on the range 50 Hz - 1 kHz. The root mean squared (RMS) output of each of the time recordings of each off the geophones is shown in Figure 5.4. It can be seen that both geophones oriented perpendicular to axis of excitation have very similar RMS voltage outputs. These are lower than either of the geophones of parallel orientation. This is to be

expected as there should be little motion of the soil in the direction perpendicular to the axis of excitation.

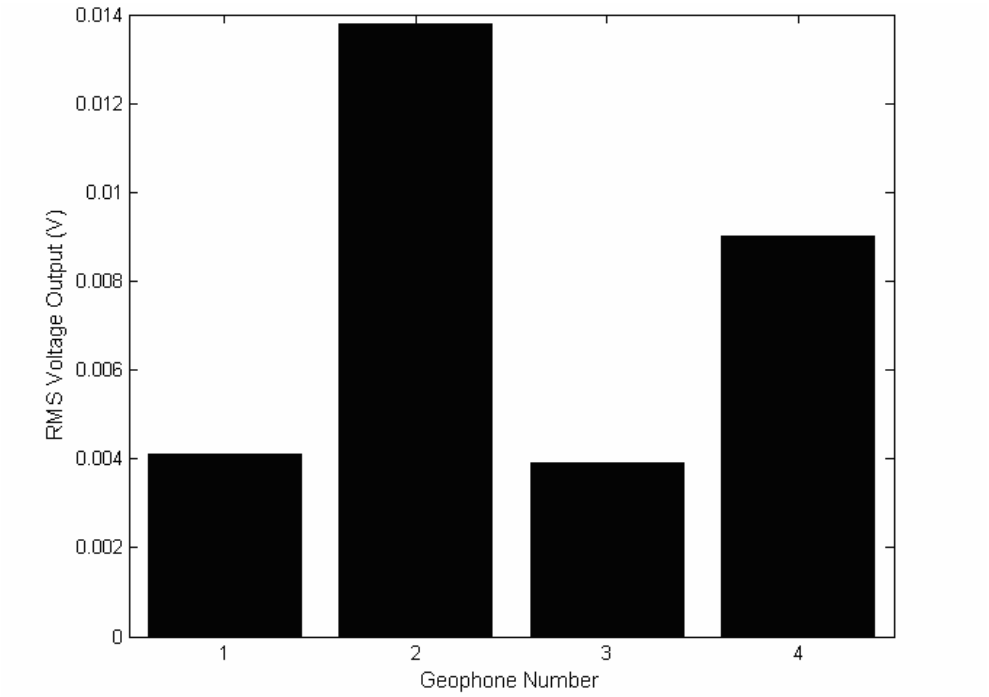

Figure 5.4 - Root mean squared voltage output of the geophones used for directivity and coupling measurement. The geophone numbers refer to the numbering in Figure 5.3.

5.4 - Surface Measurements of Ground Properties

5.4.1 - Surface Attenuation

In order to measure the attenuation of the waves as they propagate along the surface of the ground a line of geophones spaced 0.5 m apart was used, with the source located 0.25 m from end of the measurement line. Chirps in the range 50 Hz - 2 kHz were used as the excitation signal and the root mean squared value of the output of each geophone taken in order to assess the level of attenuation. Whilst transfer functions between geophone locations could be measured to obtain estimates for the surface attenuation this produced poor results. There was often no clear attenuation variation with frequency and a very high degree of variability between measurement runs, implying that the local inhomogeneities of the ground strongly influence the details of the response.

Figure 5.5 shows three plots of the RMS values of the velocity as a function of distance and their average. Each of these plots was taken from a different run on the same site, but not at the exact same location. Unlike the transfer functions, the root mean square values are reasonably consistent and thus a more useful measure of the attenuation. There is attenuation in velocity of approximately 11 dB per metre. The last two geophones have similar levels of RMS velocity, which is likely to be due to noise. The signal seems to fall below the noise floor from about 1.75 m.

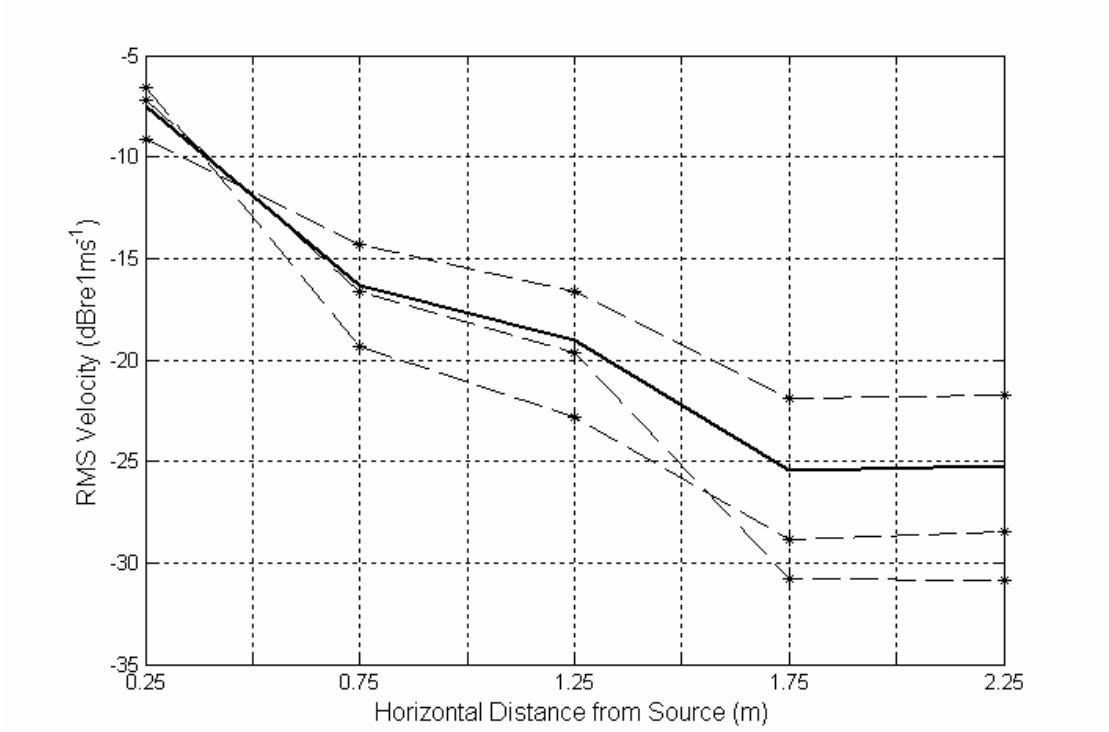

Figure 5.5 - Plot of the dB magnitude of the velocity RMS measured at geophones as a function of the geophone distance from the target. Dashed lines show three examples from different locations and the solid line their average.

5.4.2 - Surface Wavespeed Measurements

There are two techniques that are used and critically compared when obtaining wavespeed measurements. Both require the experimental setup shown in Figure 5.6. The setup consists of two measurement lines of three geophones each. The measurement lines ran perpendicular and parallel to the axis of excitation, with all geophones measuring in the horizontal plane and parallel to the axis of excitation. The geophones were spaced equidistantly with an interval of 0.5 m.

The first method uses the gradient of the unwrapped phase of the transfer function between geophones. Consider the spatial part the phase of a harmonic propagation, kx . For a fixed geophone separation of D the phase can be expressed as

$$\varphi = \frac{D\omega}{c}, \tag{5.1}$$

where c is the desired wavespeed. Differentiation with respect to frequency and rearrangement yields the expression for the wavespeed in terms of the gradient of the phase of

$$c = 2\pi D\left(\frac{d\varphi}{df}\right)^{-1}. \tag{5.2}$$

The unwrapped phase is robust to noise contamination [63] and thus provides data to much higher frequencies than can be obtained from the magnitude information.

Within this range for ideal non-dispersive transmission over a single path the phase of the transfer function phase should be linear. In reality this will not be the case for a variety of reasons, including reflections, different types of wave propagation, dispersive propagation and inhomogeneities in the ground.

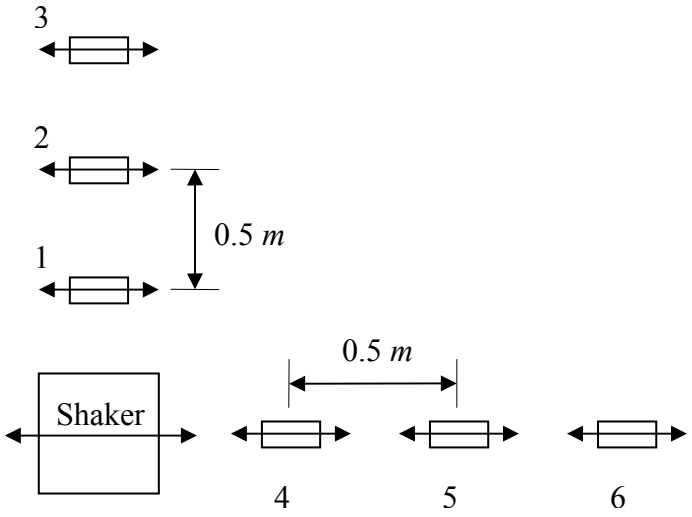

Figure 5.6 - Diagram of the experimental setup used to make the surface wavespeed measurements. Arrows indicate the axis of excitation of the shaker and axis of sensitivity of the geophones.

The geophones located inline with the direction of excitation are considered first (denoted as geophones 1 to 3 in Figure 5.6). The unwrapped phase of the transfer function between the first and second geophones is shown in Figure 5.7. It is evident that the unwrapped phase of the transfer function deviates substantially from the linear ideal. Three small regions of approximate linearity can be observed in the Figure 5.7, between 55-70 Hz, 200-250 Hz and 280-340 Hz. These give wavespeeds of 37 ms^{-1}, 65 ms^{-1} and 150 ms^{-1} respectively. It is clear that the large variation in gradient over the frequency range in which the phase can be successfully unwrapped prevents accurate estimation of the wavespeed.

As three geophones were used there are three possible combinations of transfer function. These give similar results; an unwrapped phase with little linear behaviour giving very variable wavespeed prediction.

The three geophones located in a line perpendicular to the direction of excitation (denoted as geophone 4 to 6 in Figure 5.6) are now considered. The unwrapped phase of these is closer to the ideally linear response and thus enables an estimation of the wavespeed over a wider frequency range. Figure 5.8 shows the unwrapped phase of the transfer function between the fourth and sixth geophones. Using the gradient of the approximately linear region shown by the dashed line a wavespeed of 98 ms^{-1} is obtained.

The results from the other two possible combinations are 94 ms^{-1} and 106 ms^{-1} for the fourth to fifth and fifth to sixth geophones respectively, giving a mean of 99 ms^{-1} and a standard deviation of 6 ms^{-1}.

The second method that can be used to obtain an estimate for the wavespeed is via the use of cross-correlation functions, as outlined in Section 4.5. The basic cross-correlation function is used with windowing in the frequency domain to minimise the effects of high frequency electrical noise. The maximum value of the cross-correlation function is taken to correspond to the time delay between the signals measured on the two geophones. The process of estimating the wavespeed using cross-correlation functions can be completely automated with no need for subjective decisions, as in the case for estimating the gradient of the unwrapped phase of the transfer functions. The results are summarised in Table 5.1, with the results obtained from the transfer function method shown for comparison. It can be seen that both methods give consistent results, with the cross-correlation method having the smaller of the standard deviations.

Geophones	**Wavespeed Estimate via Transfer Function (ms^{-1})**	**Wavespeed Estimate via Cross-Correlations (ms^{-1})**
1^{st} & 2^{nd}	N/A	71
1^{st} & 3^{rd}	N/A	77
2^{nd} & 3^{rd}	N/A	77
Mean	**N/A**	**75**
Std. Deviation	**N/A**	**2.8**
4^{th} & 5^{th}	94	85
4^{th} & 6^{th}	98	91
5^{th} & 6^{th}	106	99
Mean	**99**	**92**
Std. Deviation	**6.4**	**5.9**

Table 5.1 - Measured wavespeeds along the surface of the ground using both the gradient of the unwrapped phase of the transfer function and the cross-correlation method.

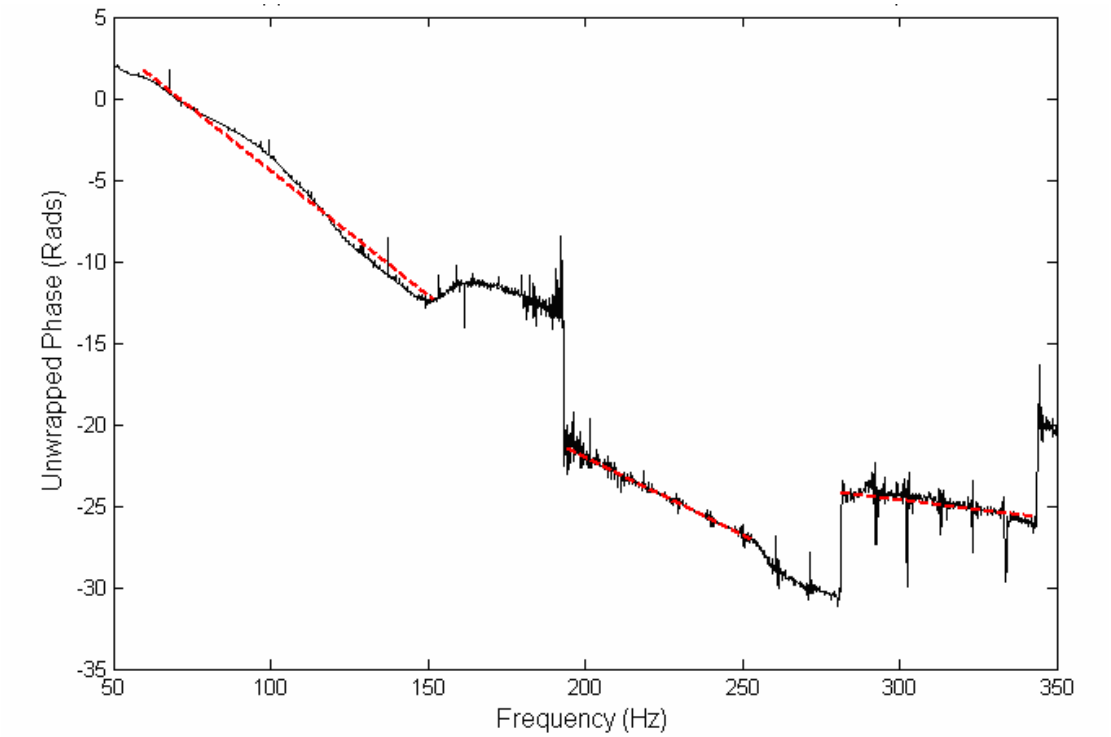

Figure 5.7 - Plot of the unwrapped phase of the transfer function between the first and third geophones. Geophone separation was 1 m and the excitation signal a linear chirp ranging from 50 Hz to 1 kHz. The dashed line shows the regions of approximate linearity.

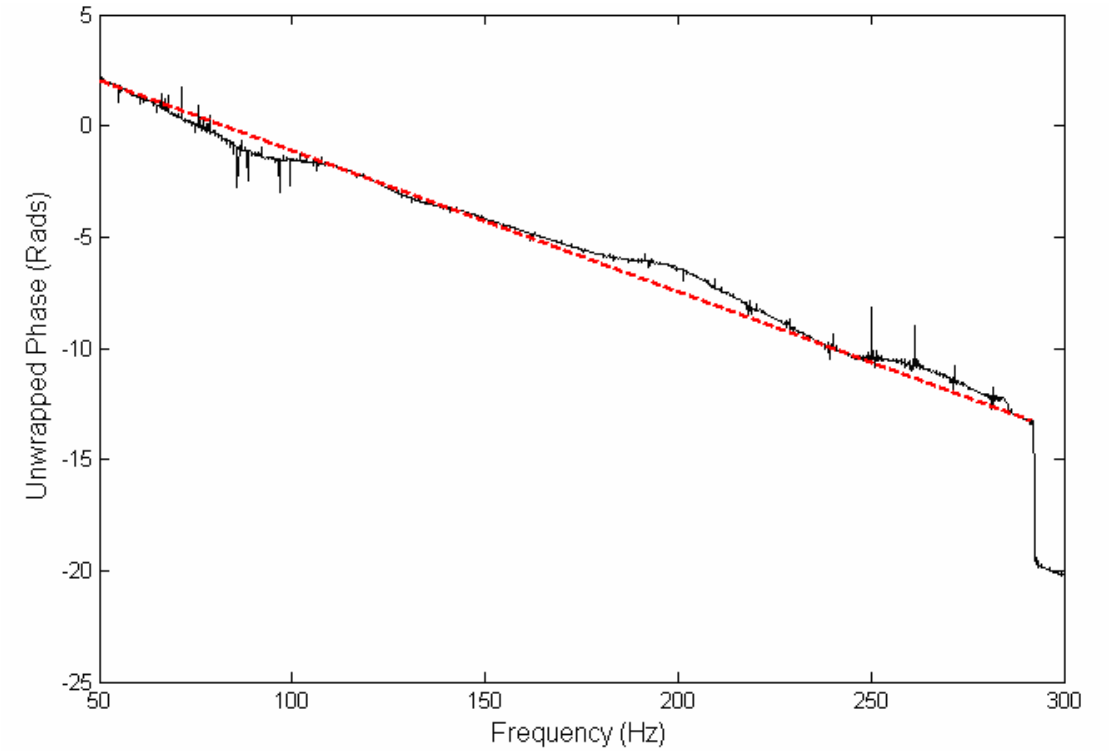

Figure 5.8 - Plot of the unwrapped phase of the transfer function between the fourth and sixth geophones. Geophone separation was 1 m and the excitation signal a linear chirp ranging from 50 Hz to 1 kHz. The dashed line shows the linear approximation taken.

5.4.3 - Discussion of Surface Measurements

The two wavespeed measurements produce broadly consistent results, and both have their own advantages. The transfer function method has the ability to clearly show if the wavespeed alters with frequency, either due to dispersive wave propagation or to the dominance of particular wave types in certain frequency ranges. The transfer function method also gives an indication of the frequency limits of the signal reaching the sensor by failing to unwrap the phase for low signal to noise ratios. It does however require subjective input in order to decide on the regions of linearity and in approximating this linearity.

The cross-correlation method has the advantage that its implementation can be automated, with no need for subjective input. In addition, or perhaps because of this, the cross-correlation method seems to give more consistent results. However by measuring only the peak of the cross-correlation function, the resultant information is compressed to a single numerical output rather outputted as a function of frequency. Whilst it is possible to ascertain if the cross-correlation behaviour represents dispersive wave propagation [37], this is, for the complex correlation functions involved, not practical.

The cross-correlation method thus provides less information about the details of the wave propagation but does enable automation of the measurement. For this reason both measurements should ideally be taken; the cross-correlation measurements to obtain values for the wavespeeds and the transfer function method to examine the wavespeeds over the frequency range.

It can be seen from the measurements shown in Table 5.1 that the surface wavespeeds in the two orthogonal directions parallel and perpendicular to the direction of excitation of the shaker platform consistently differ. This observation can be explained by noting that propagations of compression travel at higher velocities than those of shear. Although this behaviour does not fit with the simple model of ground propagation in Section 2.2 it can be expected that the wavespeed measurements in a direction and geophone orientation that measure compression should give a higher value than for the measurements in a direction and geophone orientation that measure shear.

5.5 - Pipe Transducer Measurements of Ground Properties

In addition to the surface geophones an accelerometer was attached to the inside of the buried pipe. Whilst the ability to locate a transducer on the target will not be available in real application of the method it is very useful for experimental trials. This is because it enables measurement of the waves propagating through the ground, not just along its surface. Thus one can examine the body waves with minimal interference from the surface waves and furthermore assess the properties of the ground directly, rather than trying to ascertain them indirectly through the surface wave measurements.

5.5.1 - Pipe Transducer Transfer Functions

An accelerometer was attached to piece of wood that was glued to the upper inside surface of the pipe in order to achieve adequate coupling. The output of the accelerometer was then passed to a charge amplifier located in the pipe, and the

output of this was then sent to the data acquisition. The shaker and platform were located approximately above the location of the pipe accelerometer and linear acceleration chirps with frequency content in the range of 50 Hz to 2 kHz were used as the excitation waveform. The magnitude of the transfer function between the shaker and pipe accelerometers is shown in Figure 5.9 for the shaker platform orientated in the shear position. It can be seen that there is an attenuation of approximately 4 dB per octave over the frequency range of 50 Hz to 800 Hz. The most notable deviation from this approximation is at 200 Hz, where the attenuation peaks at over 10 dB above the general trend. This may be due to a local inhomogeneity. Considering only the lowest frequencies the attenuation as a function is depth is approximately 20 to 25 dB per metre.

The magnitude of the transfer function between the shaker and pipe accelerometers for the shaker exciting in a compressional manner is shown in Figure 5.10. It can be seen that the attenuation is closer to the ideal of exponential increasing with increasing frequency. The attenuation value is estimated to be 5 dB per octave, although it should be noted that the overall attenuation compared to the shear oriented shaker is still less at all frequencies. Considering only the lowest frequencies the attenuation as a function is depth is approximately 15 to 20 dB per metre.

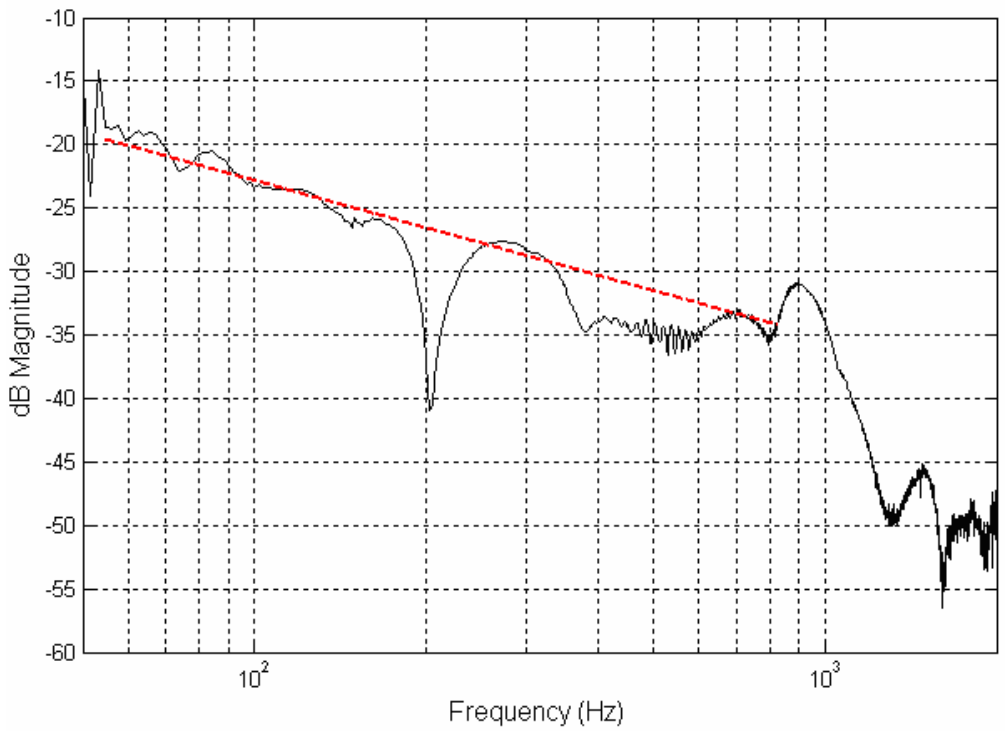

Figure 5.9 - Magnitude of the transfer function between the shaker and pipe accelerometer for the shaker in the shear excitation position.

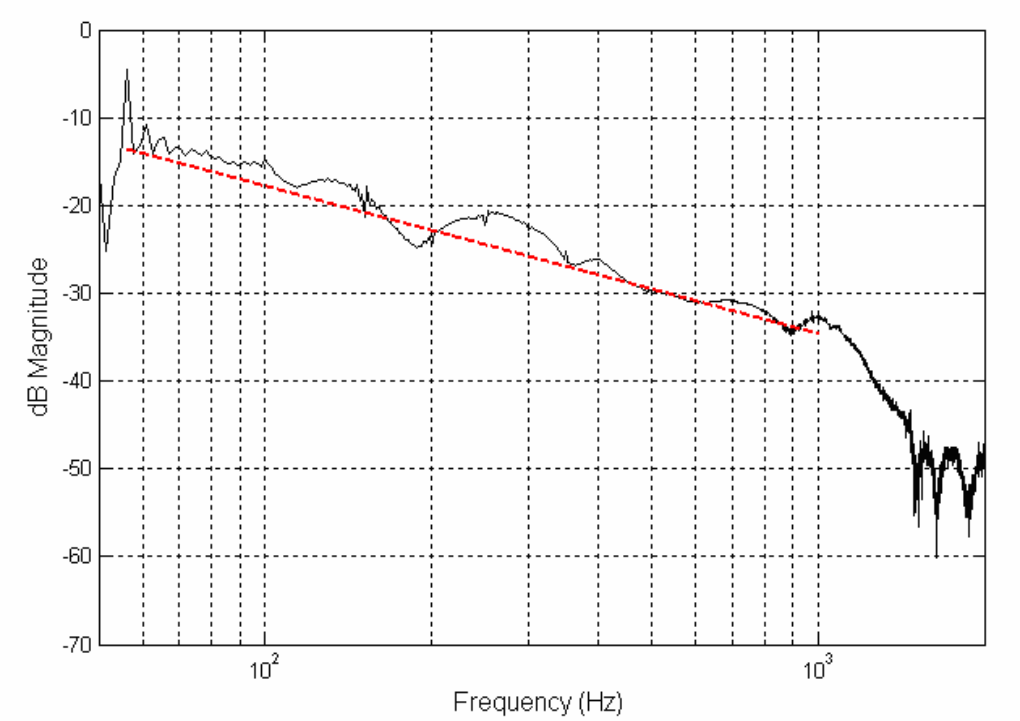

Figure 5.10 - Magnitude of the transfer function between the shaker and pipe accelerometer for the shaker in the compressional excitation position.

5.5.2 - Pipe Transducer Wavespeed Measurements

The Dataphysics acquisition unit was used for the measurement of frequency domain data taken in order to obtain transfer functions. Linear chirps generated by the Dataphysics acquisition unit in the frequency range of 50 Hz to 2 kHz were used as an input. The measurement was averaged over 20 recordings and the resultant unwrapped phase of the transfer function between the shaker accelerometer and the pipe accelerometer shown in Figure 5.11. It is immediately apparent that there the transfer function phase is much cleaner than those obtained from surface measurements. This appears mainly to be because the Dataphysics unit was less susceptible to the electrical noise which was prominent when the Prosig unit is used.

The phase of the transfer function can be unwrapped over the whole range of input frequencies. As the pipe was buried at a depth of approximately 1 m this means that the phase can be unwrapped for through ground propagation to higher frequencies than for surface propagation over the same distance. This is due to the extra noise in the surface measurements. If a linear approximation is taken over the larger range of phase unwrapping from 200 Hz to 1600 Hz then a wavespeed of 300 ms^{-1} is obtained. This value shall be critically analysed in the proceeding section.

For time domain data measurements taken in order to obtain cross-correlation functions the Prosig data acquisition unit was used. Figure 5.12 shows the cross-correlation function between the shaker accelerometer and the pipe accelerometer signals. The peak in the cross-correlation function occurs at a time of 3.4 ms which implies a wavespeed of approximately 295 ms^{-1}, assuming that the pipe was buried at a depth of 1 m.

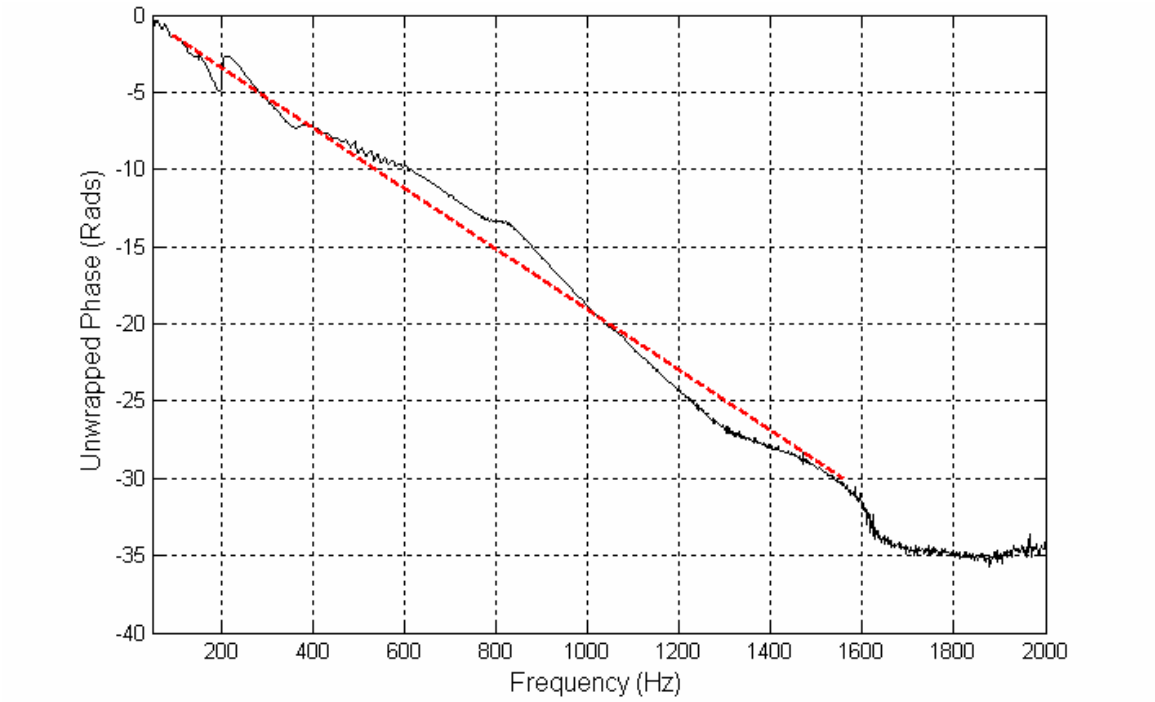

Figure 5.11 - Plot of the unwrapped phase of the transfer function between the shaker and pipe accelerometers. The dashed line denotes the approximation to linear behaviour.

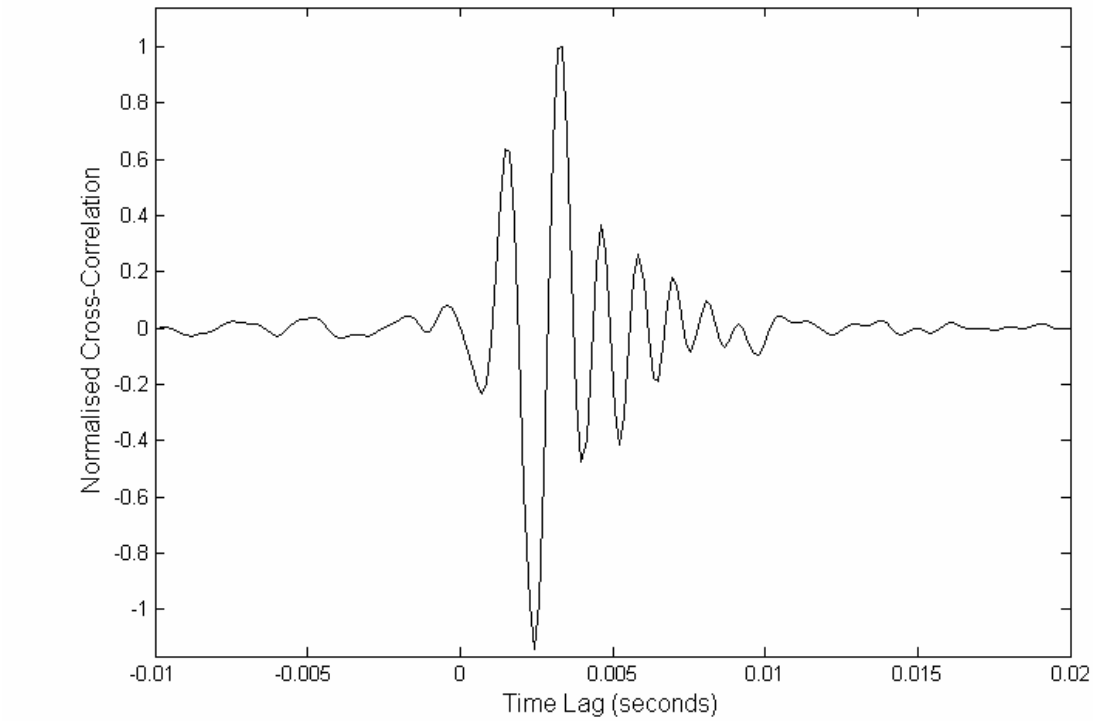

Figure 5.12 - Plot of the basic cross-correlation function between the shaker and pipe accelerometers.

5.5.3 - Discussion of Pipe Transducer Measurements

The speed of the waves propagating through to the ground to the pipe accelerometer is inconsistent with the estimates obtained in Section 5.4.2. For the soil type at the site (clay) the Poisson's ratio should be approximately 0.45 [35]. This implies a ratio of the Rayleigh to shear waves of 0.95. For a Rayleigh wavespeed of 75 ms^{-1} this gives a shear wavespeed of approximately 80 ms^{-1}. Both the transfer function and cross-correlation methods of wavespeed estimation give values far higher than this.

In order to examine the wave behaviour measured at the pipe transducer the unwrapped phase of the transfer function between the shaker and pipe accelerometer given in Figure 5.11 can be examined in greater detail. As the Rayleigh wave amplitude decreases with depth, with this reduction increasing with increasing frequency, the Rayleigh wave amplitude at the pipe will become negligible for high enough frequencies. The phase can be unwrapped at frequencies under about 1.2 kHz, corresponding to a wavelength of about 6.3 cm and therefore a depth to wavelength ratio of 16 at the pipe. From Equation 2.34 this corresponds to a reduction in Rayleigh wave amplitude of over 140 dB. It is therefore not plausible that the Rayleigh wave is responsible for the unwrapping of the phase in at least the highest linear frequency region between 800 Hz and 1.2 kHz. This phase must correspond to the measurement of a body wave.

Conversely at the lowest frequencies of 50 Hz the depth to wavelength ratio will only be about 0.7. From Equation 2.34 this corresponds to a reduction in the wave component amplitude of less than a half. As the Rayleigh wave can be expected to be of considerably higher amplitude than the body waves, the unwrapped phase of the transfer function of Figure 5.11, in this low frequency range, is likely to correspond to a Rayleigh wave. The approximately linear region between 50 and 200 Hz gives, by naïve application of Equation 5.2, a wavespeed of 190 ms^{-1}. When using this equation it should however be noted that the distance to be used is the propagation distance. As Rayleigh waves are surface waves, the wavespeed associated with them refers only to their propagation speed along the surface of the ground, not through it. The waves are evanescent with respect to depth, and therefore decay with depth rather than propagate downwards.

The assumption will be made that the Rayleigh wave displacements occur virtually simultaneously at all depths, with further theoretical investigations required to lift this assumption. This implies that if the shaker and accelerometer pipes were exactly vertically aligned the gradient of the unwrapped phase should be zero, as there would be no time delay at any frequency. The fact that it has been measured otherwise implies that there may have been a notable horizontal distance between the shaker and the pipe accelerometer during measurement. This is a likely scenario given that the location of the pipe was not known exactly from the surface. Equation 5.2 can be rearranged to give the propagation distance given the wavespeed. Using the result from the surface wavespeed measurements of Section 5.4.2 this implies a propagation distance of about 40 cm. This is a plausible result.

If the shaker and pipe transducer were misaligned by about 40 cm this would correspond to a body wave propagation distance of about 1.1 m. The unwrapped phase of the transfer function in the frequency region 800 Hz to 1.2 kHz thus implies a wavespeed of 260 ms^{-1}. This differs from the cross-correlation function wavespeed

measurement. This is because the cross-correlation measurement takes all frequency information into account and therefore effectively averages the wavespeed of all wave propagations. This explains why there is such good agreement between the cross-correlation result and the transfer function results in the previous section where a linear average was taken over the whole frequency range of phase unwrapping. Due to the presence of multiple wave types the cross-correlation method is therefore not suited to the measurement of wavespeeds to buried sensors.

The wavespeed values obtained are consistent with the propagating body wave being compressional. From the relations between wavespeeds given in Section 2.2 a Poisson's ratio of 0.45 implies a ratio of the Rayleigh to compressional wavespeeds of about 0.28 [64]. For the Rayleigh wavespeeds measured in Section 5.4.2 of 75 ms^{-1} this gives a compressional wavespeed of 265 ms^{-1}. This is consistent with the results obtained for the propagation speed of the body wave. It is therefore likely that the dominant wave being measured by the pipe transducer is the compressional, not the shear wave.

This result is unexpected as the excitation platform was specifically designed to maximise shear wave excitation and because only a small portion of the input energy should go into compressional excitation. The implied shear wavespeed has been stated to be about 80 ms^{-1}. A shear wave reaching the pipe transducer would therefore be expected to give a peak in the time delay at about 12 ms. There is no such peak visible in Figure 5.12. It is therefore likely that the shear wave is of very small amplitude and its associated correlation peak obscured by the peak associated with the compressional and Rayleigh waves.

5.6 - Stacking Method Measurements

5.6.1 - Parameter Set-up & Data Processing

For the implementation of the stacking method the Prosig data acquisition unit was used in order to provide the greatest number of input channels. Six geophones were used, with one channel used for a reference geophone and one for recording the signal from the shaker accelerometer. A geophone spacing of 0.5 m was chosen, giving a total measurement line of length 2.5 m. A smaller geophone separation would result in the measurement line being of comparable dimensions to the target and the target would therefore effectively form a subsurface rather than a point object. A larger geophone separation would, due to the high ground attenuation, cause the signal to noise ratio on the furthest geophones to be too low to be of use.

The excitation signal was chosen in be a linear chirp with frequency content in the range of 50 Hz to 2 kHz. Due to the use of a standard signal generator only acceleration chirps could be produced. This has the effect of immediately reducing the bandwidth of the signals measured at the geophones, as the geophones measure velocity, not acceleration. Although this unavoidably leads to an increase in the width of the cross-correlation peaks (see Section 4.2.2) it was mandated by equipment limitations on the experimental site.

When considering the duration of the chirp it would be considered useful for the duration to be less than the propagation time, as this would enable the direct and reflected waves to be separated in the time domain. However as the propagation distances involved in shallow object detection are only of order of a few meters the time of flight is very small; only a few milliseconds. If the chirp were to be compressed into such a short time duration the output is likely to be affected by the transient response of the shaker. As such the length of the chirp can be chosen somewhat arbitrarily provided it does not exceed the limits of the shaker. A longer input signal is preferable as it enables more energy to be inputted into the system. Rather than have a single long chirp it was decided to have a chirp of duration one second and have many repeats of the chirp. Ten repeats were used throughout the following experimental work.

In order to activate the data acquisition unit was triggered to record when the signal from the reference geophone exceeded a limit set just above the noise floor. A pre-trigger of a tenth of a second was set to ensure that all time domain data was captured, and a further tenth of a second added to the recording length over the ten seconds allowed for the chirp to ensure that all reflections were also recorded. The sample rate was set at 40 kHz. This was set well above that required for the measurement of the frequency components of interest to enable fine resolution in the time domain such that the very short time intervals could be measured accurately. As memory on the acquisition unit and post-processing equipment was abundant the high sample rate could be achieved without compromising on performance.

The captured data was filtered prior to any processing. For this a third order IIR Chebyshev filter was used, filtering in the range of 50 Hz to 1.2 kHz. The filter range was not extended to the upper limit of the input signals' frequency content. This is because it was found that the high ground attenuation at these frequencies prevented an adequate signal to noise ratio for this portion of the signal to be beneficial in forming the images. In order to eliminate the phase distortion caused by IIR filtering

the signal was passed through the filter, reversed, and then passed through the filter again. This has the effect of cancelling out the phase distortion of the filter and doubling the effective order of the filter [59]. It is important to eliminate phase distortion as the cross-correlation relies on the phase of the signals in order to estimate the relative time delay.

For reasons described in Section 3.3.1 it is necessary to envelope the cross-correlation functions prior to their stacking. Enveloping was achieved via the use of the Hilbert transform [59, 65]. The Hilbert transform is defined, for a signal $x(t)$ by

$$\tilde{x}(t) = x(t) \otimes \frac{1}{\pi t},$$

where $\otimes$ denotes convolution and $\tilde{(\,)}$ the Hilbert transform of a function. The envelope of the signal $x(t)$ is obtained by the finding the magnitude of the analytic signal [59]. The analytic signal, x_A, is defined by the sum of signal with its Hilbert transform multiplied by the square root of minus one;

$$x_A = x(t) + j\tilde{x}(t),$$

$$\Rightarrow Env(x(t)) = \sqrt{x(t)^2 + \tilde{x}(t)^2}\,.$$

where *Env* denoted the envelope of the signal. The enveloped signals were then cross-correlated with the phase transform applied and images formed using the stacking procedure described in Section 3.

5.6.2 - Results & Discussion

For the first implementation of the method the measurement line was set perpendicular to the run of the pipe in order to obtain a cross-sectional image of the pipe. The measured time histories are shown in Figure 5.13, where geophones one to six are the measurement geophones and geophone seven is the reference geophone. It can be seen that the amplitude of the time domain signal rapidly reaches small levels as the frequency increases. Furthermore there are no reflections visible in the time domain data.

The application of the cross-correlation of the geophone signals with the reference is shown in Figure 5.14. The peaks around a time lag of zero, which are particularly visible in the first and second geophones, are due to the electronic noise in the system being correlated with itself. They are more prominent in the furthest geophones due to the lower signal to noise ratio. Whilst there are some peaks which could be reflections, there are none that could be said to represent a pipe reflection with confidence.

By stacking the cross-correlation functions an image of the target can be obtained. This is shown in Figure 5.15. The location of the pipe is clearly visible in the image at the expected location. In order to show the importance of using generalised cross-correlation functions Figure 5.16 shows an image obtained in an identical method to

that shown in Figure 5.15, except that rather than using the phase transform the basic cross-correlation function has been used. The spatial resolution is very poor and spurious targets are visible. The SCOT transform can also be used instead of the PHAT, but serves only to produce a virtually identical image for increased computational complexity. It should be noted that in order to produce these images the data from the geophones closest to the each side of the source were excluded. This was done in order to eliminate the geophone data most contaminated by the surface wave.

Whilst the method has been successful in the image shown, in other measurement runs with the same experimental setup images of the target were not produced. In some spurious targets are visible whilst in others there is broad intersection of the parabolas that form the image. This is because the signal to noise ratio of the reflected wave is too low, most likely due to both the high noise levels and high surface wave amplitude relative to the reflected wave. The result of these poor images is that summing multiple images taken with different excitation positions does not necessarily enhance the detection of the image. An image formed by stacking two successful implementations is shown in Figure 5.17. It can be seen that by summing multiple stacking images of good quality the spatial resolution and on/ off target image contrast is enhanced.

The experiment was also performed with the measurement line parallel to the run of the pipe. Thus the pipe should effectively form a subsurface. An identical experimental and post processing procedure was performed with the resultant image shown in Figure 5.18. For this experiment it was found that the stacking of images produced by multiple runs was necessary in order to illuminate the length of the target. The run of the pipe can be seen at the correct depth, with the maximum of the image being at the centre. This is because the centre of the pipe, over all excitation positions, is closer to the source and thus can be expected the have the greatest level of reflected signal.

When evaluating the stacking method used it should be remembered that the method only forms a cross-sectional image in a single plane. Energy reflected from outside this plane of measurement will also be detected by the geophones and feature in the cross-correlation functions, but will not be accounted for by the algorithm and thus have a detrimental effect on the quality of the resultant image. The problem of reflected energy can expected to be more prominent when the measurement line is perpendicular to the run of the pipe, as there will be a greater distance between the measurement plane and the location of the reflector.

A possible contributory factor to the low signal to noise ratio of the reflected waveform is the nature of the target; an extended object. A notable portion of the incident waveform may go into the excitation of motion along the pipe, rather than reflecting. The use of a target with convex curvature will also diminish the signal to noise ratio of the received waveform, as the reflected wave will be scattered in many directions.

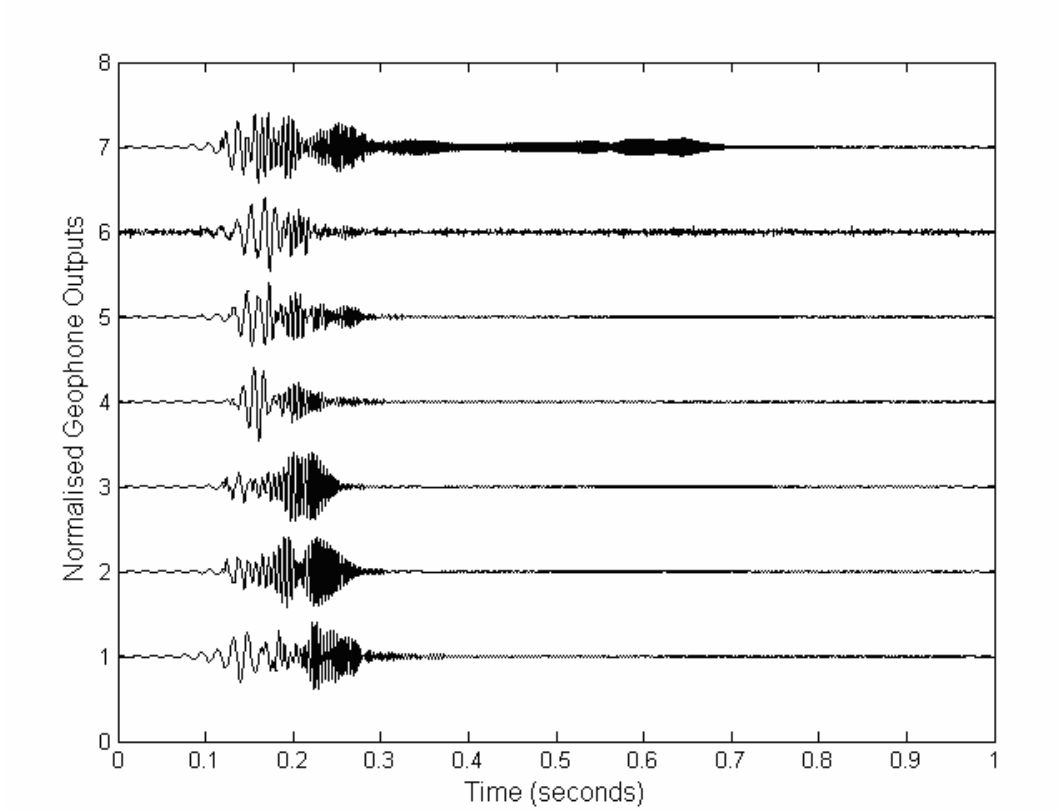

Figure 5.13 - Plots of the time domain geophone outputs for measurement line over pipe. Geophones one to six are measurement geophones and geophone 7 is the reference signal geophone.

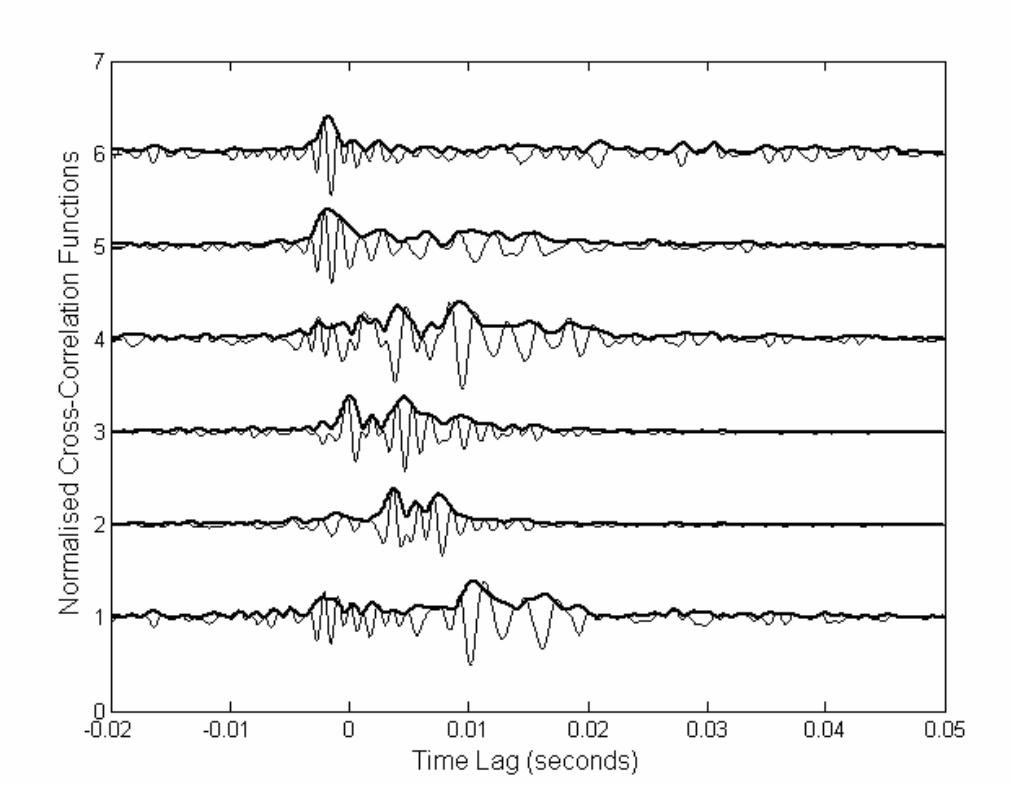

Figure 5.14 - Plots of the cross-correlation functions of the geophone signal with the reference geophone. The envelope function used is shown by the bold line and obtained via the Hilbert transform.

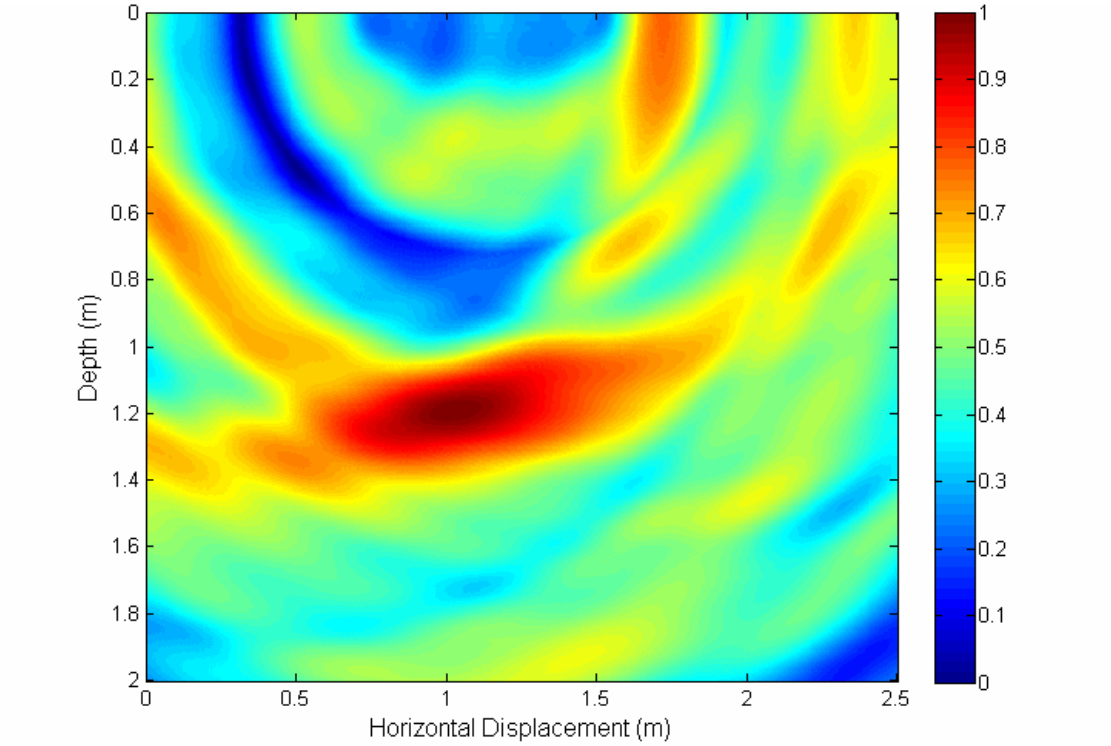

Figure 5.15 - Image produced by the stacking of the enveloped cross-correlation functions shown in Figure 5.14. The phase transform was applied and all signals filtered in the with a pass band between 50 Hz and 1.2 kHz. The compressional wavespeed was set at 270 ms^{-1}. The source was located at 0.75 m. The pipe run is perpendicular to the measurement line.

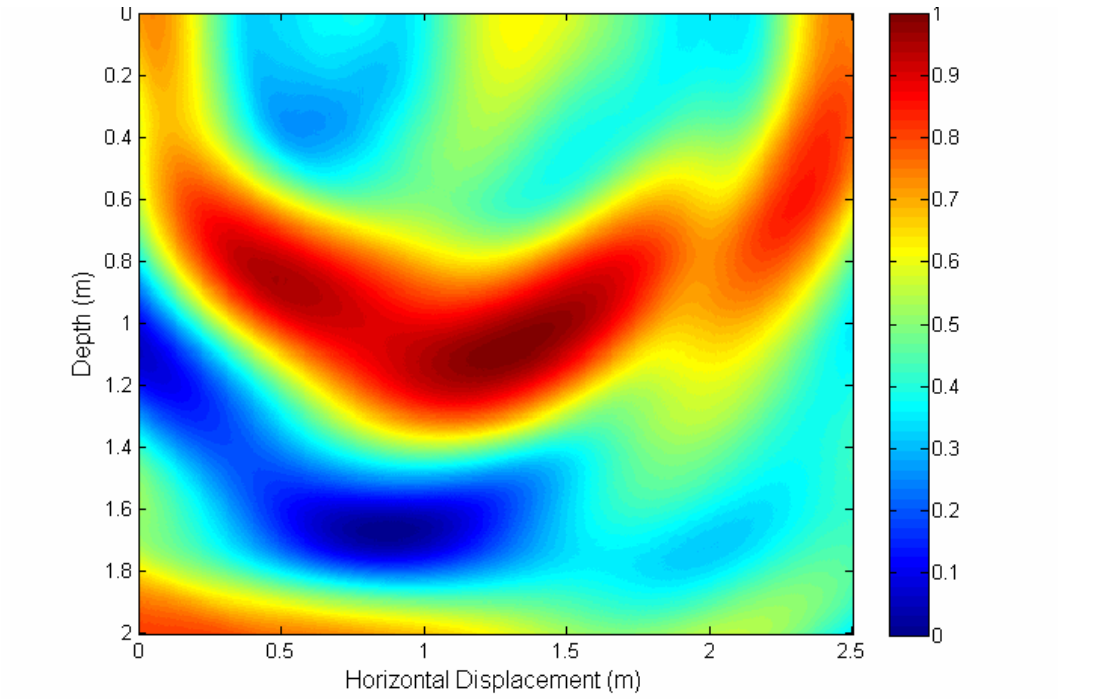

Figure 5.16 - Image produced identically to that in Figure 5.15 but with only basic cross-correlation functions.

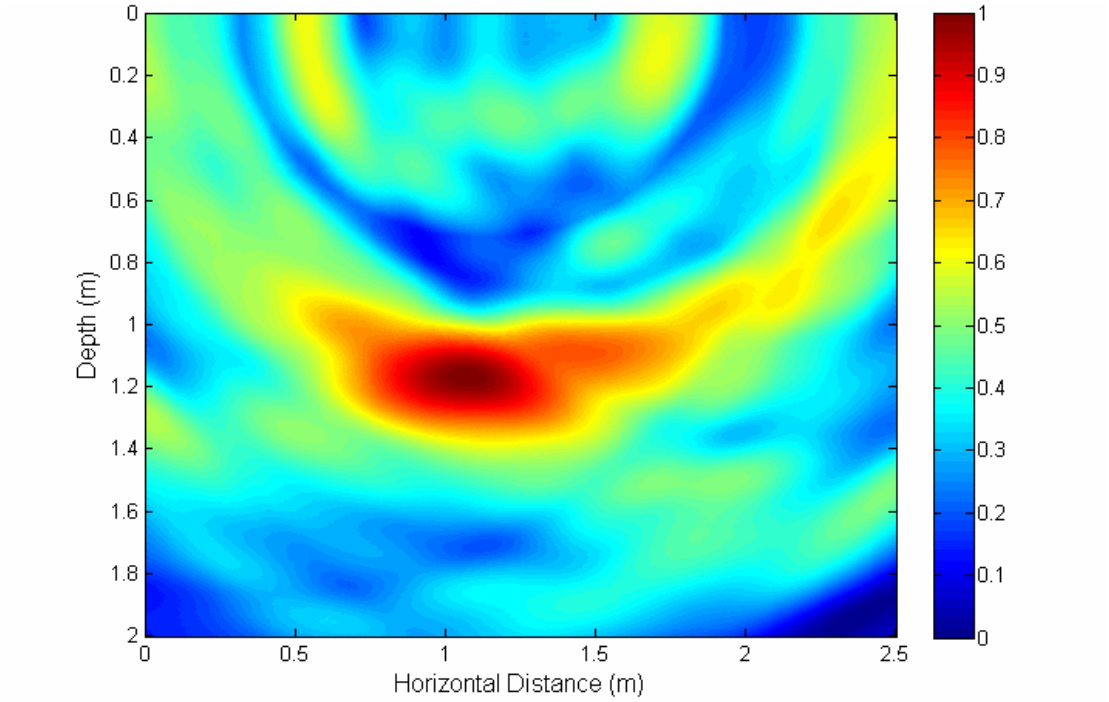

Figure 5.17 - Sum of two stacking images formed by data from two different shaker locations - 0.75 m and 1.75 m.

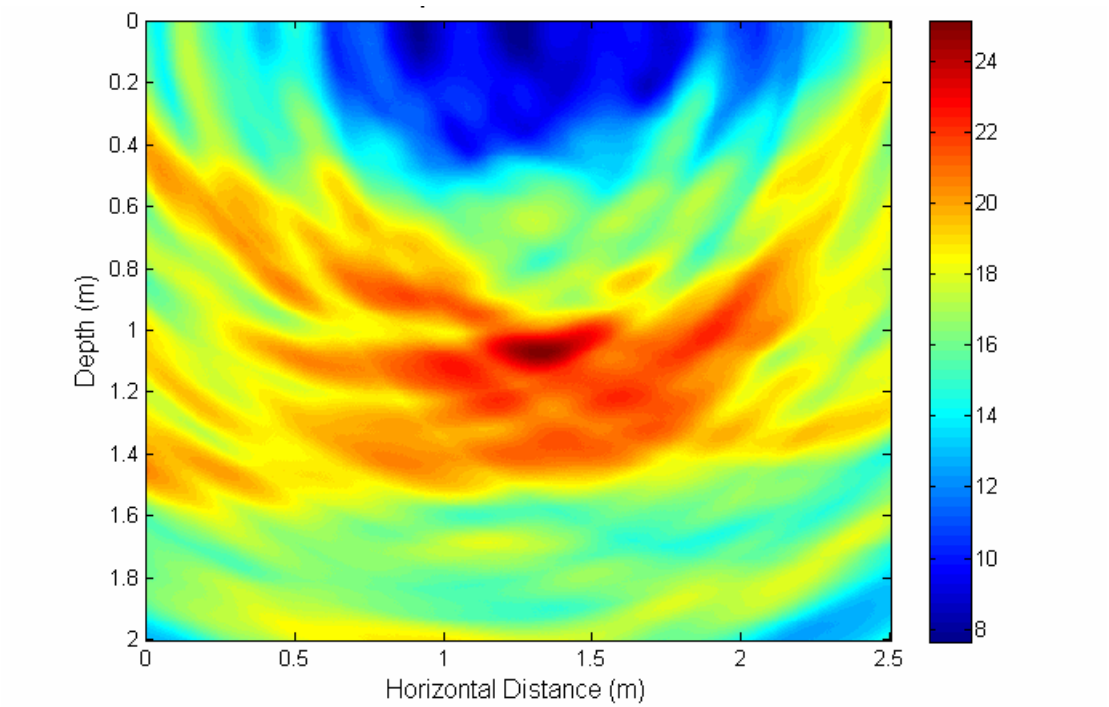

Figure 5.18 - Image produced by a sum of the stacking method images for five platform positions. The phase transform was applied and all signals filtered in the with a pass band between 50 Hz and 1.2 kHz. The compressional wavespeed was set at 270 ms^{-1}. The pipe run is parallel to the measurement line.

6. Conclusions and Future Work

The well established theoretical background to ground vibrations has been reviewed, and the time domain stacking method described and expanded upon by the use of extended time signals. This mandates the use of stacking in the cross-correlation domain rather than the time domain. As such a review of both basic and generalised cross-correlation functions has been given, with specific attention paid to the practical problem of bandwidth limitations. Shear waves are recommended for target detection throughout to maximise the time of flight between the reflected body wave and unavoidable surface wave.

The experimental work undertaken in an attempt to detect a concrete pipe succeeded in measuring the compressional and Rayleigh wavespeeds using both cross-correlation functions and the gradient of the unwrapped phase of transfer functions. Their relationship has been found to be consistent with the theoretical predictions. The shear wave has, however, not been detected in any measurements at the target, despite a shaker platform design specifically aimed to achieve maximum shear wave propagation. As such the correlation domain stacking has been modified to account for compressional wave reflections from the target.

By stacking correlation functions assuming compressional wave reflections propagating with a speed of 270 ms^{-1} a cross-sectional image of the target can be obtained. Without application of the phase transform to the cross-correlations there is poor spatial resolution and spurious images. The detection of the target even with the phase transform is not reliable and the target is not visible in all measurement runs. Measurements parallel to the pipe such that it forms an effective subsurface using an identical method to the cross-sectional experiment succeed in detecting the target and the properties of the resultant image can be elaborated upon.

In order to improve the correlation domain stacking method additional techniques and modifications have been considered that will form the basis of future work. A method used and recommended by other authors [42] is that of phase reversal of signals. This involves every measurement being performed twice with the phase of the input signal reversed. Addition or subtraction of the two measurements may cause cancellation of the some wave components, improving the signal to noise ratio of the desired reflected wave.

A possible cause of the unreliable image quality has been noted as reflections from outside the plane of measurement. These will still be measured by the geophones and correlated favourably with the reference signal. In order to overcome this problem it would be necessary to increase the aspect ratio of the shaker platform. By orientating the platform dimension parallel to the measurement line the directivity pattern of the platform should ensure that maximal energy is inputted into the plane of measurement.

The use of velocity chirps, whilst recommended in Section 4, was not possible in the experimental work due to problems with high noise levels. This immediately lowered the bandwidth of the signals, thus increasing the width of the cross-correlation peaks and reducing image quality. The deliberate boosting of the high frequency components relative to the low frequency portion of the chirp should also be

considered with the aim of countering attenuation and therefore reducing the correlation peak widths.

A method that features prominently in underwater detection of objects is beamforming [48]. Beamforming consists of a similar experimental setup to the stacking method and uses a line array of sensors. The output of these sensors is summed, exploiting the directivity of the collection of sensors, even if they are individually omnidirectional. By introducing phase shifts and amplitude weightings into the recorded signals before summation the direction and width of the beam can be controlled. This method is generally designed with far-field and narrowband constraints which would need to be lifted before application to the seismic problem.

A useful experiment to be included in future work is the use of a buried excitation source. This could be attached to an existing buried object such as the inside of a pipe. The use of an underground source would enable the body waves reaching the surface to be measured in isolation without being obscured by surface waves. The complex interaction of body waves with the free surface, which is not fully understood, could be examined in detail, resulting in possible improvements to the method.

Finally any future work must include further experiments. In shallow seismic detection the assumptions made in the theoretical analysis are frequently seriously violated, resulting in substantial deviations between expected and observed behaviour. To have confidence in the method the above additions should be included and the experimentation repeated with the aim of increasing the reliability of the imaging method. Furthermore the method should be applied to the detection of non-extended objects to examine its ability to find more localised targets.

Section 7 - Appendices

Appendix A - Basic Elasticity

In this appendix a brief review of the basic theory of elasticity shall be given. This section will cover only material required for this document. A much more detailed review can be found in one of the many excellent books on the topic, for example those by authors such as Timoshenko [56] and Kolsky [55].

A.1 - Preliminary discussion and definitions

Throughout the following section a standard Cartesian coordinate system is used. A general elastic body exists in a space defined by coordinates x, y and z, with deformation displacements of the body denoted by u, v and w, corresponding to the three coordinates respectively. The vectors $\boldsymbol{x}$ and $\boldsymbol{u}$ are used to denote a point and a displacement in the space with respect to the origin respectively. Where generality is required or index notation is used Latin subscripts are applied to these vectors to denote a non-specific dimension. For example $\partial u_i / \partial x_i$ would denote differentiation of a non-specified displacement component with respect to its associated spatial coordinate.

For the following analysis, the elastic body is assumed to be perfectly elastic and therefore returns exactly to its original shape after deformation without hysteresis effects. The body is also assumed to be homogeneous and isotropic. Body forces (those which act throughout the volume of the body) and hydrostatic forces (those which act equally over the surface of the body) are also neglected.

A.2 - Stress & Strain

Stress is defined as the force per unit area that acts internally within a body. When the direction of the force is perpendicular to a surface the stress is referred to as a normal stress and is denoted by σ_i, where the subscript refers to the plane in which the surface exists. Forces acting perpendicular to the surface are referred to as shear stresses and are denoted by τ_{ij}, where the first subscript refers to the plane in which the surface exists and the second to the direction in which the force is exerted.

Strain is defined as the fractional change in length of a body under deformation. Axial strain concerns extension perpendicular to the surface of the body and shear strain extension in a direction parallel to the body surface. In order to obtain a relation for axial strain consider two points on a one dimensional element of length dx_i. Let one end of the element at an arbitrary location x_i be displaced by an amount $u_i(x_i)$. At the other end of the element at $x_i + dx_i$ the displacement is given by $u_i(x_i + dx_i)$. By carrying out a Taylor series expansion for small dx_i to find the extension of the element and then dividing by the original length the axial strain in the x_i dimension, ε_{x_i}, can be obtained as

$$\varepsilon_i = \frac{\partial u_i}{\partial x_i}. \qquad \text{(A.1)}$$

Relations for the shearing strains can be found by considering two elements existing in the dimensions x_i and x_j and defined by OA and OB. These are initially considered to be perpendicular and then subject to a deformation such that *O*, *A* and *B* are transformed to O', A' and B'. It is assumed that the deformations do not result in a change in length of the elements (i.e. there is no axial strain). The displacements of the elements are shown in Figure A.1. The displacements of the end points containing partial differentials can be obtained by carrying out a Taylor series expansion as before or by considering the geometry of the system under small angle approximations. The angular deflection of the elements are therefore $\partial u_j / \partial x_i$ and $\partial u_i / \partial x_j$.

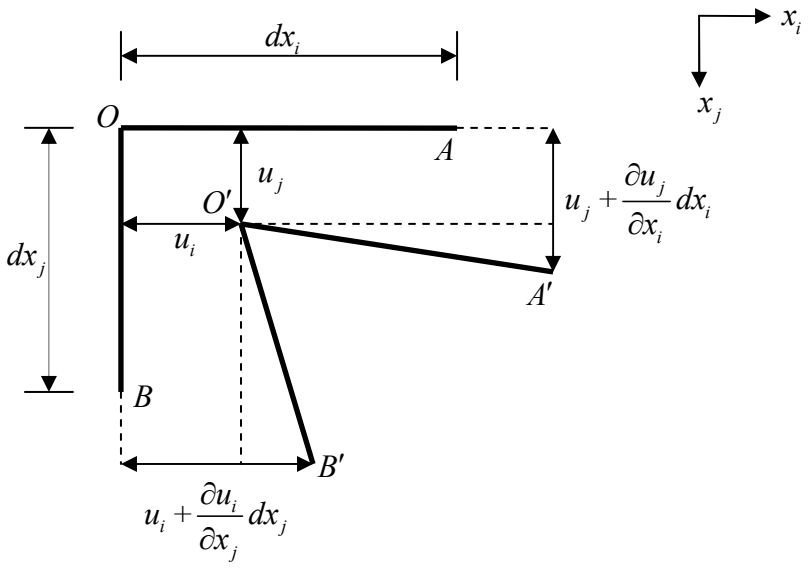

Figure A.1 - Diagram used to illustrate the derivation of the shear strains. Application of shear deforms two elements defined by OA and OB to $O'A'$ and $O'B'$ respectively.

The shear strain is denoted by γ_{ij}, where the first subscript denotes the dimension plane in which the surface exists and the second the dimension in which the extension takes place. The shear strain is equal to the sum of the angles of deformation. Thus

$$\gamma_{ij} = \frac{\partial u_i}{\partial x_j} + \frac{\partial u_j}{\partial x_i} . \tag{A.2}$$

A.3 - Hooke's Law

It is empirically observed that for some materials under small deformations that the normal stress and strain are proportional

$$\varepsilon_x = \frac{\sigma_x}{E} , \tag{A.3}$$

where the constant of proportionality, E, is usually referred to as the Young's modulus. It is intuitive to expect that an axial extension of a body will lead to axial compression in the two other dimensions. Assuming proportionality and isotropicity this effect is described by;

$$\varepsilon_y = \varepsilon_z = -\nu\frac{\sigma_x}{E}, \tag{A.4}$$

where the constant of proportionality, ν, is referred to as the material's Poisson's ratio. The negative sign is necessary to account for the fact that extension in one direction will lead to compression in others. In order to combine these extensions into a single expression for a body under an axial load principle of superposition is applied. Thus the three equations describing the extension in a given direction in terms of the applied axial stresses are given by;

$$\varepsilon_i = \frac{1}{E}\left[\sigma_i - \nu\left(\sigma_j + \sigma_k\right)\right]. \tag{A.5}$$

It is can also be assumed that, provided deformations are small, the shear strain is proportional the shear stress;

$$\gamma_{ij} = \frac{\tau_{ij}}{G}, \qquad i \neq j, \tag{A.6}$$

where G is referred to as the shear modulus. The shear modulus can be expressed purely in terms of the existing proportionality ratios as follows [56];

$$G = \frac{E}{2\left(1+\nu\right)}. \tag{A.7}$$

Equation A.5 is often rewritten in terms of the axial stresses. Rearrangement of Equation A.5 yields;

$$\sigma_i = \mu\varepsilon + 2G\varepsilon_i. \tag{A.8}$$

where $\mu = \nu E\left[\left(1+\nu\right)\left(1-2\nu\right)\right]^{-1}$ and the non-subscripted $\varepsilon = \frac{\partial u_i}{\partial x_i} + \frac{\partial u_j}{\partial x_j} + \frac{\partial u_k}{\partial x_k} = \nabla \bullet \mathbf{u}$.
Collectively the constants μ and G are known as the Lamé constants.

Appendix B - Derivation of the Cross-Correlation Function of Bandlimited Signals

For real values signals the auto-spectral density is an even function. As such a one sided auto-spectral density, $G_{xy}(f)$ is defined [66] as

$$G_{xx}(f) = \begin{cases} 2S_{xx}(f) & f > 0 \\ S_{xx}(f) & f = 0 \\ 0 & f < 0 \end{cases}. \tag{B.1}$$

Consider only the region of positive frequencies. Recalling that the auto-spectral density and the auto-correlation form a Fourier transform pair (Section 4.2.1), the cross-correlation can be expressed as the inverse Fourier transform of the one sided auto-spectral density:

$$R_{xx}(\tau) = F^{-1}\{S_{xx}(f)\} = 2F^{-1}\{G_{xx}(f)\}. \tag{B.2}$$

As $R_{xx}(-\tau) = R_{xx}(\tau)$ the auto-correlation function has even symmetry and the Fourier transform therefore reduces to the Fourier cosine transform:

$$R_{xx}(\tau) = \int_0^\infty G_{xx}(f)\cos(2\pi f\tau)df\ . \tag{B.3}$$

The definition of the one sided spectra therefore enables calculation of the auto-correlation. For a bandlimited signal this is given by

$$G_{xx}(f) = \begin{cases} M & f_0 - b/2 \le f \le f_0 + b/2 \\ 0 & \text{elsewhere} \end{cases}, \tag{B.4}$$

where M is the amplitude of the signal in the transmission band, f_0 is the centre frequency of the band and b is the bandwidth. Substitution of Equation B.4 into Equation B.3 with the cosine of the latter equation converted to complex exponential form yields

$$R_{xx}(\tau) = M\int_{f_0-b/2}^{f_0+b/2} e^{j2\pi ft}df + M\int_{f_0-b/2}^{f_0+b/2} e^{-j2\pi ft}df\ . \tag{B.5}$$

Performing the integration and substituting in the limits;

$$R_{xx}(\tau) = \frac{M}{4j\pi\tau}\left\{\left[e^{j2\pi\tau(f_0+b/2)} - e^{j2\pi\tau(f_0-b/2)}\right] - \left[e^{-j2\pi\tau(f_0+b/2)} - e^{-j2\pi\tau(f_0-b/2)}\right]\right\}. \tag{B.6}$$

Rearranging the exponential arguments;

$$R_{xx}(\tau) = \frac{M}{4j\pi\tau}\left\{e^{j2\pi\tau f_0}\left[e^{j\pi\tau b} - e^{-j\pi\tau b}\right] + e^{-j2\pi\tau f_0}\left[e^{j\pi\tau b} - e^{-j\pi\tau b}\right]\right\}. \quad \text{(B.7)}$$

Finally using the complex exponential definition of sine and cosine functions the result reduces to

$$R_{xx}(\tau) = Mb\,\mathrm{sinc}\left[\pi\tau b\right]\cos\left[2\pi\tau f_0\right]. \quad \text{(B.8)}$$

For a cross-correlation with a perfectly delayed and scaled version of the waveform the result of Equation 4.9 can be applied yielding the final result that for a delay τ_0 and scaling factor C between input signal $x(t)$ and output signal $y(t)$ the cross-correlation function is

$$R_{xy}(\tau) = MbC\,\mathrm{sinc}\left[\pi b(\tau - \tau_0)\right]\cos\left[2\pi f_0(\tau - \tau_0)\right]. \quad \text{(B.9)}$$

8. References

1. MacDonald, J., *Alternatives for Landmine Detection*. 2003: RAND Corporation.

2. Griffiths, *Introduction to Electrodynamics*. 3rd ed. 1981: Prentice Hall.

3. Bruschini, C., *Metal detectors in civil engineering and humanitarian de-mining: Overview and tests of a commercial visualizing system.* Insight: Non-Destructive Testing and Condition Monitoring, 2000. **42**(2): p. 89-97.

4. Das, Y., *Effects of soil electromagnetic properties on metal detectors.* IEEE Transactions on Geoscience and Remote Sensing, 2006. **44**(6): p. 1444-1453.

5. Eblagh, K. *Practical problems in demining and their solutions*. 1996. Edinburgh, UK: IEE.

6. Vales, B.R., et al. *Moisture effects in soils using a frequency domain metal detector*. 2007. Budapest, Hungary: Institute of Electrical and Electronics Engineers Computer Society, Piscataway, NJ 08855-1331, United States.

7. Gebicke, M.E., *Mine Detection: Army Detector's Ability to Find Low-Metal Mines Not Clearly Demonstrated*, U.S.G.A. Office, Editor. 1996.

8. Krueger, H., et al. *Advanced signal processing for reduction of false alarm rate of metal detectors for humanitarian mine clearance*. 2006. Sorrento, Italy: IEEE.

9. Won, I.J., D.A. Keiswetter, and T.H. Bell, *Electromagnetic induction spectroscopy for clearing landmines.* IEEE Transactions on Geoscience and Remote Sensing, 2001. **39**(4): p. 703-9.

10. Huang, H., et al., *Coaxial coil towed EMI sensor array for UXO detection and characterization.* Journal of Applied Geophysics, 2007. **61**(3-4): p. 217-226.

11. Daniels, D.J., D.J. Gunton, and H.F. Scott, *Introduction to Subsurface Radar.* IEE Proceedings, 1988. **135, Pt. F** (4): p. 278 - 320.

12. Metje, N., et al., *Mapping the Underworld - State-of-the-art Review.* Tunnelling and Underground Space Technology, 2007. **22**: p. 568-586.

13. Van der Merwe, A. and I.J. Gupta, *A novel signal processing technique for clutter reduction in GPR measurements of small, shallow land mines.* IEEE Transactions on Geoscience and Remote Sensing, 2000. **38**(6): p. 2627-37.

14. Marion, J. and M. Heald, *Classical Electromagnetic Radiation*. 1980: Academic Press.

15. Daniels, D.J., *A review of GPR for landmine detection.* Sensing and Imaging, 2006. **7**(3): p. 90-123.

16. Garroway, A.N., et al., *Remote sensing by nuclear quadrupole resonance.* Geoscience and Remote Sensing, IEEE Transactions on, 2001. **39**(6): p. 1108-1118.

17. Gasser, R. and T.H. Thomas. *Prodding to detect mines: a technique with a future*. 1998. Edinburgh, UK: IEE.

18. Acheroy, M. *Mine action: status of sensor technology for close-in and remote detection of antipersonnel mines*. 2005. Delft, Netherlands: IEEE.

19. Suess, H., et al. *Investigations on anti-personal mine detection using microwave radiometers*. 2001. Sydney, NSW: Institute of Electrical and Electronics Engineers Inc.

20. Martin, J.S., G.D. Larson, and W.R. Scott Jr, *An investigation of surface-contacting sensors for the seismic detection of buried landmines.* Journal of the Acoustical Society of America, 2006. **120**(5): p. 2676-2685.

21. Scott, W., Jr., J.S. Martin, and G.D. Larson, *Experimental model for a seismic landmine detection system.* IEEE Transactions on Geoscience and Remote Sensing, 2001. **39**(6): p. 1155-1164.

22. Scott, W.R., Jr., C. Schroeder, and J.S. Martin. *A hybrid acoustic/electromagnetic technique for locating land mines*. 1998. Seattle, WA, USA: IEEE.

23. Sabatier, J. and K. Gilbert, *Method for Detecting Buried Objects By Measuring Seismic Vibrations Induced by Acoustical Coupling with a Remote Source of Sound*, U.S.P. Office, Editor. 2000: United States.

24. Sabatier, J.M., et al., *Acoustically induced seismic waves.* Journal of the Acoustical Society of America, 1986. **80**(2): p. 646-9.

25. Sabatier, J.M., et al., *The interaction of airborne sound with the porous ground: the theoretical formulation.* Journal of the Acoustical Society of America, 1986. **79**(5): p. 1345-52.

26. Donskoy, D., et al., *Nonlinear seismo-acoustic land mine detection and discrimination.* Journal of the Acoustical Society of America, 2002. **111**(6): p. 2705-14.

27. Zagrai, A., D. Donskoy, and A. Ekimov, *Structural vibrations of buried land mines.* Journal of the Acoustical Society of America, 2005. **118**(6): p. 3619-3628.

28. Richart, Hall, and Woods, *Vibrations of Soils and Foundations*. 1970: Prentice-Hall.

29. Cook, J.C. and J.J. Wormser, *Semi-Remote Acoustic, Electric, and Thermal Sensing of Small Buried Non-Metallic Objects.* IEEE Transactions on Geoscience Electronics, 1973. **GE-11**(3): p. 135-152.

30. Biot, M., *Theory of Propagation of Elastic Waves in a Fluid-Saturated Porous Solid. II. Higher Frequency Range.* Journal of the Acoustical Society of America, 1956. **28**(2): p. 179-191.

31. Bellan, F., et al., *(Non-Linear) Acoustic Landmine Detection Study*. 2004, EUDEM2.

32. Arnott, W. and J. Sabatier, *Laser-Doppler Vibrometer Measurements of Acoustic to Seismic Coupling.* Applied Acoustic, 1990. **30**: p. 279-291.

33. Xiang, N. and J.M. Sabatier, *An experimental study on antipersonnel landmine detection using acoustic-to-seismic coupling.* Journal of the Acoustical Society of America, 2003. **113**(3): p. 1333-41.

34. Fokin, V.N., et al., *Effect of ground variability on acoustic-to-seismic transfer function and false alarms in landmine detection.* Journal of the Acoustical Society of America, 2006. **120**(2): p. 621-30.

35. Pinnington, R., *Feasibility Study to Investigate the Detection of Objects Buried in the Ground*. 1996, ISVR, University of Southampton.

36. Grice, R. and R. Pinnington, *The Detection of Objects Buried in Sand Using Vibrations Generated by Shakers Located at the Sand Surface: Results of Experimental Investigations in the Laboratory*. 1997, ISVR, Univeristy of Southampton.

37. White, P., *Cross Correlation in Structural Systems: Dispersion and Nondispersion Waves.* Journal of the Acoustical Society of America, 1969. **45**(5).

38. House, L. and D. Pape, *Method and Apparatus for Acoustic Energy Identification of Objects Buried in Soil*. 1994: United States.

39. Sugimoto, T. and M. Okujima, *Underground Imaging Using Shear Waves: Stacking Method of the Reflected Scattered Waves* Japanese Journal of Applied Physics, 1996. **35**: p. 3105-3108.

40. Sugimoto, T., H. Saito, and M. Okujima, *Improvement of underground image: Underground imaging using shear waves.* Japanese Journal of Applied Physics, Part 1: Regular Papers & Short Notes & Review Papers, 1997. **36**(5B): p. 3197-3198.

41. Sugimoto, T. and H. Saitou, *Improvement of Underground Image (II): Underground Imaging Using Shear Waves.* Japanese Journal of Applied Physics, 1998. **37**: p. 3120-3121.

42. Sugimoto, T., H. Saitou, and M. Okujima, *Study of Underground Imaging Using Shear Waves: the Stacking Method of the Reflected Scattered Wave.* Archaeological Prospection, 2000. **7**: p. 249-261.

43. Yoshizumi, N. and T. Sugimoto, *Improvement of Underground Image (III): Underground Image Using Shear Waves.* Japanese Journal of Applied Physics, 2001. **40**: p. 3621-3622.

44. Schnieder, W.A., *The Common Depth Point Stack.* Proceedings of the IEEE, 1984. **72**(10): p. 1238 - 1256.

45. Donskoy, D., et al., *Nonlinear Vibrations of Buried Mines.* Journal of the Acoustical Society of America, 2005. **117**(2): p. 690-700.

46. Korman, M.S. and J.M. Sabatier, *Nonlinear acoustic techniques for landmine detection.* Journal of the Acoustical Society of America, 2004. **116**(6): p. 3354-69.

47. Knight, W.C., R.G. Pridham, and S.M. Kay, *Digital signal processing for sonar.* Proceedings of the IEEE, 1981. **69**(11): p. 1451-1506.

48. Burdic, *Underwater Acoustic System Analysis*. 1984: Prentice-Hall.

49. Thorner, J.E. *Approaches to sonar beamforming*. 1990. Binghamton, NY, USA: IEEE.

50. Schock, S.G., et al., *Buried object scanning sonar.* IEEE Journal of Oceanic Engineering, 2001. **26**(4): p. 677-89.

51. Schmidt, R.O., *Multiple emitter location and signal parameter estimation.* IEEE Transactions on Antennas and Propagation, 1986. **AP-34**(3): p. 276-80.

52. Schickert, M., *Progress in ultrasonic imaging of concrete.* Materials and Structures/Materiaux et Constructions, 2005. **38**(283): p. 807-815.

53. Schickert, M., M. Krause, and W. Muller, *Ultrasonic imaging of concrete elements using reconstruction by synthetic aperture focusing technique.* Journal of Materials in Civil Engineering, 2003. **15**(3): p. 235-246.

54. Barton, *Modern Radar System Analysis*. 1988: Artech House.

55. Kolsky, *Stress Waves in Solids*. 1963: Dover Publications.

56. Timoshenko, S., *Theory of Elasticity*. 1st ed. 1934: McGraw-Hill

57. Graff, K., *Wave Motion in Elastic Solids*. 1991: Dover Publications.

58. Rayleigh, J.W.S., *The Theory of Sound*. 1945: Dover Publications.

59. Shin and Hammond, *Fundamentals of Signal Processing for Sound and Vibration Engineers*. 2008: John Wiley & Sons.

60. Knapp, C.H. and G.C. Carter, *The generalised correlation method for estimation of time delay.* IEEE Transactions on Acoustics, Speech and Signal Processing, 1976. **ASSP-24**(4): p. 320-7.

61. Karl, L., W. Haegeman, and G. Degrande, *Determination of the material damping ratio and the shear wave velocity with the Seismic Cone Penetration Test.* Soil Dynamics and Earthquake Engineering, 2006. **26**(12): p. 1111-1126.

62. Graff, K., *Wave Motion in Elastic Solids*. 1975: Dover Publications.

63. Muggleton, J., M. Brennan, and Y. Gao, *Determining the Location of Underground Plastic Water Pipes from Measurements of Ground Vibration.* Unplublished Journal Article.

64. Ewing and Jardetzky, *Elastic Waves in Layered Media*. 1957: McGraw-Hill.

65. Johansson, M., *The Hilbert Transfrom*, Vaxjo University, Masters Thesis in Mathematics / Applied Mathematics.

66. Bendat and Piersol, *Engineering Applications of Correlation and Spectral Analysis*. 1993: John Wiley & Sons.